

Symmetry-enriched criticality in a coupled spin ladderSuman Mondal^{1,*}, Adhip Agarwala^{2,†}, Tapan Mishra^{3,4,‡} and Abhishodh Prakash^{5,§}¹*Institut für Theoretische Physik, Georg-August-Universität Göttingen, D-37077 Göttingen, Germany*²*Department of Physics, Indian Institute of Technology, Kanpur 208016, India*³*School of Physical Sciences, National Institute of Science Education and Research, Jatni 752050, India*⁴*Homi Bhabha National Institute, Training School Complex, Anushaktinagar, Mumbai 400094, India*⁵*Rudolf Peierls Centre for Theoretical Physics, University of Oxford, Oxford OX1 3PU, United Kingdom*

(Received 28 September 2023; accepted 28 November 2023; published 12 December 2023)

We study a one-dimensional ladder of two coupled XXZ spin chains and identify several distinct gapless symmetry-enriched critical phases. These have the same unbroken symmetries and long-wavelength description, but cannot be connected without encountering either a phase transition or other intermediate phases. Using bosonization, we analyze the nature of their distinction by determining how microscopic symmetries are manifested in the long-wavelength fields, the behavior of charged local and nonlocal operators, and identify the universality class of all direct continuous phase transitions between them. One of these phases is a gapless topological phase with protected edge modes. We characterize its precise nature and place it within the broader classification. We also find the occurrence of “multiversality” in the phase diagram, wherein two fixed phases are separated by continuous transitions with different universality classes in different parameter regimes. We determine the phase diagram and all its aspects, as well as verify our predictions numerically using density matrix renormalization group and a mapping onto an effective spin-1 model.

DOI: [10.1103/PhysRevB.108.245135](https://doi.org/10.1103/PhysRevB.108.245135)**I. INTRODUCTION**

One of the most remarkable characteristics of quantum and classical many-body physical systems is the emergence of distinct, stable *phases* that are divided by sharp *phase transitions*. There is tremendous theoretical and experimental interest in enumerating all possible phases and transitions and characterizing their properties. Symmetries have provided a guiding principle to facilitate this. It was realized that distinct phases of matter occur when microscopic symmetries are spontaneously broken at long distances [1]. The knowledge of microscopic symmetries allows us to enumerate the different ways it can be spontaneously broken, the properties of the resulting long-range order, and sometimes even the nature of the phase transition. The concept of “topological” ordering that falls outside the symmetry-breaking framework [2] following the discovery of the quantum Hall effect [3] has expanded the mechanisms by which distinct phases can arise. This has spurred a flurry of intense research activity over the past decades in classifying and characterizing gapped phases of matter [4]. These new phases represent multiple ways in which symmetries can be unbroken and yet result

in different phases. The distinguishing features are detectable in subtle signatures present in entanglement patterns and boundary/topology effects.

Gapless phases, on the other hand, have been left by the wayside in these recent developments. Despite being ubiquitous in nature and making frequent appearances in the phase diagrams of many known physical systems, the mechanisms by which they arise and are stabilized are relatively unclear although various descriptive frameworks have been successfully devised to understand them. For example, when noninteracting bands of fermions are partially filled they lead to the formation of Fermi liquids [5], Dirac [6]/Weyl [7] semimetals. Using partons and emergent gauge fields to describe systems has also been useful in accessing non-Fermi-liquid phases [8,9]. The most systematic known mechanism is arguably the spontaneous breaking of continuous symmetries, e.g., which results in the formation of superfluids. The program of classifying gapless states of matter with unbroken symmetries is still in its early stages.

Examples of gapless states hosting edge modes have been reported in various papers [10–19] and was developed into the notion of gapless symmetry-protected topological (SPT) phases in Refs. [15,16]. This was generalized in Ref. [18] to the concept of “symmetry-enriched criticality” where the authors ask the following question: Given a critical state corresponding to a fixed universality class, how many ways can an unbroken symmetry *enrich* it? In other words, can microscopic symmetries manifest themselves in inequivalent ways at long distances when the physics is described by conformal field theory (CFT)? The authors demonstrate that the answer is yes and that distinct symmetry-enriched critical states exist that cannot be connected without encountering an

*suman.mondal@theorie.physik.uni-goettingen.de

†adhip@iitk.ac.in

‡mishratapan@niser.ac.in

§abhishodh.prakash@physics.ox.ac.uk

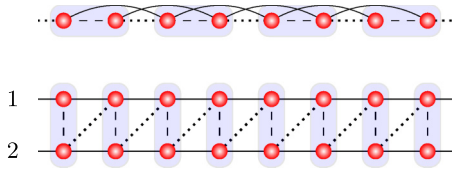


FIG. 1. Schematic representation of the Hamiltonian in the small- J limit shown in Eq. (1) (top) and the large- J limit shown in Eq. (2) (bottom). The solid and broken lines represent the various two-spin interaction terms.

abrupt change in universality class or intermediate phases. These critical states may be topological and host edge modes, or may not.

It is desirable to study models and phase diagrams, which demonstrate the existence of symmetry-enriched critical phases and transitions between them. The most common critical phases are the so-called ‘‘Luttinger liquids’’ [20], which are described by the compact-boson CFT [21] and arise as the long-wavelength description for many one-dimensional interacting systems of bosons or fermions. Coupled Luttinger liquids, which naturally arise in spin-ladder models, provide a much richer playground and will be used in this paper to investigate subtle symmetry and topological properties of gapless phases. In this paper, we study the phase diagram of a microscopic one-dimensional spin ladder that stabilizes multiple symmetry-enriched Luttinger liquid phases protected by the symmetries of the model. One of these, dubbed XY_2^* , is topological, i.e., it has stable symmetry-protected edge modes. Using Abelian bosonization, we give a comprehensive treatment of their symmetry distinction and features, as well as describe local and nonlocal observables that can differentiate between them. We also study this rich variety of phases and phase transitions numerically using density matrix renormalization group (DMRG) as well as an effective low-energy mapping to spin-1 Hamiltonians. We also discuss additional interesting features of the phase diagram such as the presence of ‘‘multiversality’’ [22,23] wherein the same two phases (Haldane and trivial) are separated by different stable universality classes in different parameter regimes.

The paper is organized as follows: In Sec. II, we introduce our model, list its symmetries, and summarize the phase diagram and its important elements. We use Abelian bosonization in Sec. III to establish the symmetry distinction between various gapless phases and in Sec. IV to analyze the topological Luttinger liquid phase XY_2^* . We numerically analyze our model in Sec. V and reproduce aspects of our phase diagram using an effective spin-1 model in Sec. VI. Various additional details are relegated to Appendices A to C.

II. MODEL HAMILTONIAN AND PHASE DIAGRAM

A. Two presentations of the model

We study a one-dimensional chain of qubits (spin halves). There are two ways to view the system. The first, shown in the top panel of Fig. 1 is to regard the system as a single chain where the Hamiltonian can be written as an XXZ chain with alternating bond strength and next-nearest-neighbor coupling as follows (the $S^z S^z$ coupling constants λ and Δ are reversed

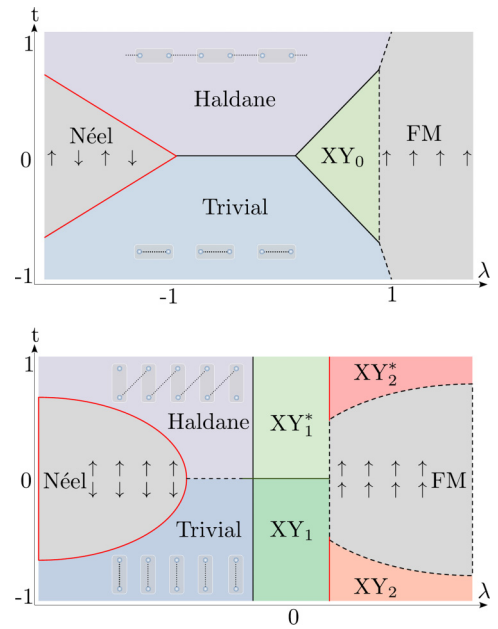


FIG. 2. The schematic phase diagram for the small- J Hamiltonian shown in Eq. (1) (top) and the large- J Hamiltonian shown in Eq. (2) (bottom). Continuous lines indicate second-order phase transitions and broken lines indicate first-order transitions. Cartoon ground states are shown for the gapped phases.

in sign compared to the usual convention for convenience):

$$H = \sum_j (1 + (-1)^j t) (S_j^x S_{j+1}^x + S_j^y S_{j+1}^y - \lambda S_j^z S_{j+1}^z) + J \sum_j (S_j^x S_{j+2}^x + S_j^y S_{j+2}^y - \Delta S_j^z S_{j+2}^z), \quad (1)$$

\vec{S}_j are spin- $\frac{1}{2}$ operators, defined as usual in terms of Pauli matrices, $\vec{S}_j = \frac{1}{2} \vec{\sigma}_j$. The model has four parameters, $\{J, \Delta, \lambda\} \in \mathbb{R}$ and $t \in [-1, 1]$. We will be interested in two-dimensional phase diagrams varying λ and t with J and Δ fixed. The representation in Eq. (1) appropriate in the limit of small J when the next-nearest-neighbor (nnn) term can be regarded as a perturbation of the bond-dimerized XXZ spin chain. The phase diagram in this limit is well known [23,24], and is schematically shown in Fig. 2. We are interested in the gapless Luttinger liquid phase labeled XY_0 , which can be adiabatically connected to the one found in the phase diagram of the XXZ model (i.e., $1/\sqrt{2} < \lambda < 1$ for $t = J = 0$).

For large J , the Hamiltonian is appropriately visualized as a two-rung spin ladder as shown in the bottom panel of Fig. 1, with the following presentation:

$$H = H_1 + H_2 + H_\perp + H'_\perp, \text{ where} \\ H_\alpha = J \sum_j (S_{\alpha j}^x S_{\alpha j+1}^x + S_{\alpha j}^y S_{\alpha j+1}^y - \Delta S_{\alpha j}^z S_{\alpha j+1}^z), \\ H_\perp = (1 - t) \sum_j (S_{1j}^x S_{2j}^x + S_{1j}^y S_{2j}^y - \lambda S_{1j}^z S_{2j}^z), \\ H'_\perp = (1 + t) \sum_j (S_{2j}^x S_{1j+1}^x + S_{2j}^y S_{1j+1}^y - \lambda S_{2j}^z S_{1j+1}^z). \quad (2)$$

TABLE I. Symmetries of the model in both the small- J and large- J representations of local operators of the Hamiltonian shown in Eqs. (1) and (2).

Symmetry	Small J	Large J
$U(1)$ spin rotations	$S_j^\pm \mapsto e^{\pm i\chi} S_j^\pm$ $S_j^z \mapsto S_j^z$	$S_{\alpha j}^\pm \mapsto e^{\pm i\chi} S_{\alpha j}^\pm$ $S_{\alpha j}^z \mapsto S_{\alpha j}^z$
\mathbb{Z}_2^R spin reflection	$S_j^\pm \mapsto S_j^\mp$ $S_j^z \mapsto -S_j^z$	$S_j^\pm \mapsto S_{\alpha j}^\mp$ $S_j^z \mapsto -S_{\alpha j}^z$
\mathbb{Z}_2^P lattice parity	$\vec{S}_j \mapsto \vec{S}_{-j+1}$	$\vec{S}_{1,j} \leftrightarrow \vec{S}_{2,-j}$
\mathbb{Z} lattice translation	$\vec{S}_j \mapsto \vec{S}_{j+2}$	$\vec{S}_{\alpha,j} \mapsto \vec{S}_{\alpha,j+1}$

$\alpha = 1, 2$ labels the rungs of the ladder and contains, respectively, the even and odd lattice spins of Eq. (1). H_α represents the intrarung and H_\perp , H'_\perp represent the interrung XXZ couplings. In this limit, it is appropriate to treat H_\perp , H'_\perp as perturbations to H_α . The schematic phase diagram in this limit, which we find is shown in Fig. 2. Our prime interest in this phase diagram are the four Luttinger liquid phases labeled XY_1 , XY_1^* , XY_2 , and XY_2^* . We will show that all five gapless phases found in the large- and small- J phase diagrams are distinct from each other meaning they cannot be connected without encountering a phase transition. Furthermore, we will also show that one of these, XY_2^* is a topological Luttinger liquid containing stable edge modes [14,18,19]. A positive finite Δ , introduces intrachain ferromagnetic correlations, which is crucial to open up various gapless phases as will be discussed in detail.

Parts of the large- J phase diagram have appeared in previous studies [25–32]. However, the complete set of gapless phases, their symmetry distinction and topological properties have not been identified to the best of our knowledge. This will be the focus of our paper. We will understand these (a) using bosonization in Secs. III and IV, (b) numerically, using density matrix renormalization group (DMRG) in Sec. V and (c) by mapping Eq. (2) to effective spin-1 models in Sec. VI.

B. Symmetries

Global symmetries of the system will play an important role. Four symmetries are sufficient to characterize all phases and transitions: (i) on-site $U(1)$ symmetry that corresponds to spin rotations, (ii) on-site \mathbb{Z}_2^R spin reflections, (iii) \mathbb{Z}_2^P lattice symmetry that corresponds to a bond-centred reflection in the small- J version and site-centred reflection followed by layer-exchange in the large- J version, and (iv) \mathbb{Z} lattice translations. The symmetry action on spin operators is shown in Table I. Altogether, the full symmetry group is [33] $G \cong O(2) \times \mathbb{Z}_2^P \times \mathbb{Z}$. Additional symmetries are present in the model (e.g., time-reversal) but are not needed for our purposes. In other words, they can be explicitly broken without changing the nature of the phase diagram.

C. Phases and transitions

The main focus of our paper are the five symmetry-enriched Luttinger liquid phases XY_0 , $XY_{1,2}$, and $XY_{1,2}^*$ shown in Fig. 2. At long distances, all five of these

are described by a compact boson conformal field theory with central charge $c = 1$. However, the presence of global symmetries results in distinctions between them. The microscopic symmetries shown in Sec. II B are imprinted on the long-wavelength degrees of freedom in different ways in each of the five phases, and as a consequence, they cannot be connected without encountering a phase transition or an intermediate phase. Conversely, the distinction can be eliminated between the phases, and they can be connected by explicitly breaking appropriate symmetries. This will be explained in detail using bosonization analysis in Sec. III.

More operationally, we will show that the distinction between these phases can be demonstrated using appropriate local and string operators. While XY_0 , XY_1 , and XY_1^* can be distinguished by local operators only, XY_2 is distinguished from XY_2^* using string operators. This is comparable to the situation with gapped phases, where symmetry-protected topological (SPT) phases [34] are distinguished by string operators. The phase diagrams shown in Fig. 2 contain a non-trivial SPT phase, the Haldane phase, which is distinguished from the trivial paramagnet using an appropriate string operator. We will see that the same string operator can be used to distinguish between XY_2 and XY_2^* . Furthermore, like the Haldane phase, the XY_2^* phase will also contain protected edge modes but with reduced degeneracy. This will also be explained in Sec. IV using bosonization and confirmed numerically in Sec. V.

We are also interested in the phase transitions between the gapless phases shown in Fig. 2. These are summarized below along with the universality class:

- (i) XY_1 to XY_1^* : $c = 2$ theory of two compact bosons.
- (ii) XY_1 to XY_2 and XY_1^* to XY_2^* : $c = \frac{3}{2}$ theory of a $c = 1$ compact boson CFT combined with a $c = \frac{1}{2}$ Ising CFT.

The second-order transitions out of the gapless phases to either the Haldane or trivial phase in Fig. 2 is of the BKT type, when the value of the Luttinger parameter is such that the perturbation that drives the gapped phase becomes relevant. We will also understand these using bosonization in Appendix B and confirm them numerically in Sec. V.

Finally, the gapped phases present in Fig. 2 (Haldane SPT, trivial paramagnet, and symmetry-breaking Néel and ferromagnet) as well as transitions between them are well understood. We mention them for completeness—The Haldane and trivial phases are separated by a compact boson CFT for small J and by a first-order transition for large J . The Néel phase is separated from the trivial and Haldane phases by an Ising CFT and its symmetry-enriched variant, respectively [18] for both small and large J . Finally, the FM is separated from the Haldane and trivial phases through a first-order transition for small J .

III. BOSONIZATION ANALYSIS I: CHARACTERIZING THE GAPLESS PHASES

In this section, we will study the properties of various gapless phases and transitions between them using Abelian bosonization. We begin by reviewing the framework applicable to the parameter regimes for small and large J and then proceed to understand the various gapless phases in two ways: (i) by using the effective action of microscopic symmetries

on the CFT and (ii) the behavior of local and nonlocal operators carrying appropriate symmetry charges. We delay a thorough analysis of the topological aspects of the XY_2^* phase to Sec. IV.

A. Bosonization formulas for small and large J and conventional description of phases

For small J , the Hamiltonian shown in Eq. (1), can be treated as a single XXZ spin chain with perturbations. In the regime of our interest, it can be bosonized using standard arguments [20,35] as follows (see Appendix A for more details):

$$H \approx \frac{v}{2\pi} \int dx \left[\frac{1}{4K} (\partial_x \phi)^2 + K (\partial_x \theta)^2 \right] + 2\mathcal{A}Ct \int dx \cos \phi - \frac{\mathcal{B}^2 \lambda}{2} \int dx \cos 2\phi + \dots \quad (3)$$

$\phi \cong \phi + 2\pi$ and $\theta \cong \theta + 2\pi$ are canonically conjugate compact boson fields with unit radii satisfying the algebra [21]

$$[\partial_x \phi(x), \theta(x')] = 2\pi i \delta(x - x'), \quad (4)$$

and $\mathcal{A}, \mathcal{B}, \mathcal{C}$ etc are bosonization prefactors whose precise values are not important. The Luttinger parameter K and the velocity v are related to the Hamiltonian parameters [36] (see Appendix A). The bosonized forms of the spin operators are

$$S_j^\pm \approx \exp(\pm i\theta(x))((-1)^j \mathcal{A} + \mathcal{C} \cos \phi(x) + \dots),$$

$$S_j^z \approx \frac{1}{2\pi} \partial_x \phi(x) + (-1)^j \mathcal{B} \sin \phi(x) + \dots \quad (5)$$

Equation 3 is a compact boson conformal field theory (CFT) with central charge $c = 1$ perturbed by vertex operators $\mathcal{U}_p \equiv \cos p\phi$ with scaling dimensions [21,37]

$$[\mathcal{U}_p] = [\cos p\phi] = p^2 K. \quad (6)$$

Note that we have only shown the most relevant operators, with the smallest scaling dimensions in Eq. (3). The ellipses ... represent other operators that are not important for our purposes. The the small- J phase diagram shown in Fig. 2 can be qualitatively reproduced from Eq. (5) by tracking the relevance [38] of \mathcal{U}_p (see Appendix B for a detailed discussion). Bond dimerization t introduces the vertex operator \mathcal{U}_1 and the interaction $S^z S^z$ while λ introduces \mathcal{U}_2 . For now, we note that in the regime when $K > 2$, all perturbations are irrelevant and correspond to the XY_0 gapless phase.

A different starting point is useful in the large- J limit. We now interpret the Hamiltonian in Eq. (2) as two XXZ spin chains with intra- and interring perturbations. Each leg can be bosonized appropriately to obtain the following two-component compact-boson theory [35]:

$$H \approx \frac{v}{2\pi} \sum_{\alpha=1,2} \int dx \left(\frac{1}{4K} (\partial_x \phi_\alpha)^2 + K (\partial_x \theta_\alpha)^2 \right) - \frac{\lambda}{2\pi^2} \int dx \partial_x \phi_1 \partial_x \phi_2 - 4\mathcal{A}^2 t \int dx \cos(\theta_1 - \theta_2) - \mathcal{B}^2 t \int dx \lambda (\cos(\phi_1 + \phi_2) - \cos(\phi_1 - \phi_2)) + 2\mathcal{C}^2 \int dx \cos(\theta_1 - \theta_2) \cos(\phi_1 + \phi_2) + \dots \quad (7)$$

where $\phi_\alpha \cong \phi_\alpha + 2\pi$ and $\theta_\alpha \cong \theta_\alpha + 2\pi$ are compact boson fields satisfying

$$[\partial_x \phi_\alpha(x), \theta_\beta(x')] = 2\pi i \delta_{\alpha\beta} \delta(x - x'), \quad (8)$$

\mathcal{A} and \mathcal{B} are again unimportant bosonization prefactors and we have only shown the most important operators. The bosonized forms of the spin operators are

$$S_{\alpha j}^\pm \approx \exp(\pm i\theta_\alpha(x))((-1)^j \mathcal{A} + \mathcal{C} \cos \phi_\alpha(x) + \dots),$$

$$S_{\alpha j}^z \approx \frac{1}{2\pi} \partial_x \phi_\alpha + (-1)^j \mathcal{B} \sin \phi_\alpha + \dots \quad (9)$$

The above theory represents a $c = 2$ CFT with perturbations. We have only retained primary [21,37] scaling operators in Eq. (9). This is sufficient to determine the structure of the phases and transitions, which is our focus. However, it is known [39] that descendant operators must be considered to understand certain *incommensurability* aspects of correlations. The large- J phase diagram can be qualitatively reproduced using Eq. (9) by carefully tracking the relevance of the operators $\mathcal{V}_\pm \equiv \cos(\phi_1 \pm \phi_2)$, $\mathcal{W}_- \equiv \cos(\theta_1 - \theta_2)$, and $\mathcal{W}_- \mathcal{V}_+ \equiv \cos(\theta_1 - \theta_2)(\phi_1 + \phi_2)$ (details of this can be found in Appendix B). Here, we again focus only on how the four gapless phases can emerge. An important fact is that the scaling dimensions of the various operators listed above are not all independent. In particular, we have $[\mathcal{V}_-] = ([\mathcal{W}_-])^{-1}$. Therefore, it is impossible for both \mathcal{V}_- and \mathcal{W}_- to be irrelevant at the same time, and for any $t \neq 0$, the $c = 2$ theory is unstable and flows to a Luttinger liquid phase with $c = 1$ or a gapped phase [26,27,35] as seen in Fig. 2. The first, which is of our main interest, occurs when all other operators, especially \mathcal{V}_+ are irrelevant. The nature of the resulting gapless phase depends on (i) which among $[\mathcal{V}_-]$ and $[\mathcal{W}_-]$ has the smaller scaling dimensions at $t = 0$. This dominates long-distance physics for $t \neq 0$ resulting in the pinning of either $\langle \phi_1 - \phi_2 \rangle$ or $\langle \theta_1 - \theta_2 \rangle$ and (ii) the value to which $\langle \phi_1 - \phi_2 \rangle = 0/\pi$ or $\langle \theta_1 - \theta_2 \rangle = 0/\pi$ is pinned, depending on the sign of t and λ . The four possibilities result in the four gapless phases shown in the large- J phase diagram of Fig. 2 as follows:

- (1) XY_1 : $[\mathcal{V}_-] > [\mathcal{W}_-]$, $\langle \theta_1 - \theta_2 \rangle = \pi$
- (2) XY_1^* : $[\mathcal{V}_-] > [\mathcal{W}_-]$, $\langle \theta_1 - \theta_2 \rangle = 0$
- (3) XY_2 : $[\mathcal{V}_-] < [\mathcal{W}_-]$, $\langle \phi_1 - \phi_2 \rangle = 0$
- (4) XY_2^* : $[\mathcal{V}_-] < [\mathcal{W}_-]$, $\langle \phi_1 - \phi_2 \rangle = \pi$.

There are two critical scenarios, which we now discuss: when $[\mathcal{V}_-] = [\mathcal{W}_-]$, the theory flows to a $c = \frac{3}{2}$ theory corresponding to a compact boson with Ising CFT [40]. For $[\mathcal{V}_-] \neq [\mathcal{W}_-]$ $t = 0$ corresponds to a phase transition described by the parent $c = 2$ two-component compact boson theory when the pinned value of the appropriate fields changes. At this stage, let us point out elements of the discussion above that already exist in the literature. The competition between $[\mathcal{V}_-]$ and $[\mathcal{W}_-]$ leading to different phases was discussed in Refs. [27,35,40]. The importance of the precise values to which the fields are pinned was appreciated relatively recently [14,18,19] where it was shown that $\langle \phi_1 - \phi_2 \rangle = \pi$ produces a gapless phase with edge modes.

However, we must be careful in using these pieces of information to conclude that we have distinct phases of matter. It was recently pointed out that this kind of distinction can disappear suddenly [22,23,41]. A more robust characterization

TABLE II. Representation of symmetries (see Table I) on the boson fields applicable in the small- J and large- J limits of the Hamiltonian shown in Eqs. (1) and (2). τ^x is the Pauli-X matrix.

	Small- J	Large- J
$U(1)$	$\theta(x) \mapsto \theta(x) + \chi$ $\phi(x) \mapsto \phi(x)$	$\theta_\alpha(x) \mapsto \theta_\alpha(x) + \chi$ $\phi_\alpha(x) \mapsto \phi_\alpha(x)$
\mathbb{Z}_2^R	$\theta(x) \mapsto -\theta(x)$ $\phi(x) \mapsto -\phi(x)$	$\theta_\alpha(x) \mapsto -\theta_\alpha(x)$ $\phi_\alpha(x) \mapsto -\phi_\alpha(x)$
\mathbb{Z}_2^P	$\theta(x) \mapsto \theta(-x) + \pi$ $\phi(x) \mapsto -\phi(-x)$	$\theta_\alpha(x) \mapsto \tau_{\alpha\beta}^x \theta_\beta(-x)$ $\phi_\alpha(x) \mapsto \pi - \tau_{\alpha\beta}^x \phi_\beta(-x)$
\mathbb{Z}	$\theta(x) \mapsto \theta(x)$ $\phi(x) \mapsto \phi(x)$	$\theta_\alpha(x) \mapsto \theta_\alpha(x) + \pi$ $\phi_\alpha(x) \mapsto \phi_\alpha(x) + \pi$

arises out of symmetry considerations, which we now turn to. We do this in two complementary ways. First, we establish the fate of the microscopic symmetries shown in Tables I and II in the deep IR for each of the gapless phases. The effective theory for all of them is that of a single compact boson. We show that in each of the five phases, the microscopic symmetries act in inequivalent ways that cannot be deformed into each other. Second, we study how appropriately charged local and nonlocal operators behave in the different phases and show a complete list of operators with distinct charges that can serve as order parameters to distinguish the different gapless phases. Our paper therefore characterizes a rather subtle interplay of symmetries and topology leading to the emergence of gapless phases.

B. Multiversality along the $t = 0$ surface

An interesting feature of the phase diagrams shown in Fig. 2 is the nature of transition separating the Haldane and trivial phases along parts of the $t = 0$ surface. In the small- J limit, we see from Eq. (3) that the critical theory corresponds to a compact boson CFT with central charge $c = 1$. In the large- J diagram, the situation is different. Consider the effective theory in Eq. (7) and set $t = 0$. This is a $c = 2$ CFT with perturbations and describes various transitions and phases along the $t = 0$ surface. In particular, the transition between XY_1 and XY_1^* corresponds to the $c = 2$ theory when all perturbations are irrelevant or tuned away. As we move along this surface, the operator $\mathcal{W}_- \mathcal{V}_+$ becomes relevant and gives us a gapped theory with two ground states, which precisely correspond to those of the Haldane and trivial phases and therefore represent a first-order transition between them (see Appendix B for a detailed discussion). Now consider the transition between XY_1 and the trivial phase. This is driven by the operator \mathcal{V}_+ becoming relevant. Since \mathcal{V}_+ has a smaller scaling dimension than $\mathcal{W}_- \mathcal{V}_+$, the XX_1 -to- trivial $c = 1$ critical line strikes the $t = 0$ line well before the first-order transition sets in. The same is true for the XY_1^* -to- Haldane transition. Consequently, we expect that a segment of the transition (close to the gapless phases) between the Haldane and the trivial phase will also be described by the $c = 2$ CFT before becoming first order as shown in Fig. 2. This situation is unusual because it is a different universality class (with a different central charge) compared to the small- J tran-

sition between the same phases. Furthermore, in both cases, the transitions are reached by tuning only a single parameter, without additional fine tuning.

The presence of multiple stable universality classes that separate the same two phases has been termed ‘‘multiversality’’ [22,23]. Although there are no physical reasons forbidding multiversality, models that exhibit it are surprisingly rare. We see that the spin-ladder model considered in this paper exhibits the phenomenon under relatively generic conditions and symmetries (compare this to the example in Ref. [23] where multiversality was observed under more restrictive symmetries and destroyed when symmetries were reduced).

C. Distinguishing gapless phases through effective symmetries

We begin this subsection by listing the action of symmetries listed in Table I on the compact boson fields in both the small and large- J versions [35,42]. This is shown in Table II and is obtained by comparing the action on the lattice operators shown in Table I with the dictionary shown in Eqs. (5) and (9) (see Appendix A for more details). We want to understand the fate of these symmetries in various gapless phases. The long-wavelength physics of each of these gapless phases is identical and corresponds to that of a single compact boson with a Hamiltonian of the form

$$H = \frac{v_{\text{eff}}}{2\pi} \int dx \left[\frac{1}{4K_{\text{eff}}} (\partial_x \phi)^2 + K_{\text{eff}} (\partial_x \theta)^2 \right]. \quad (10)$$

How do the microscopic symmetries act on the long wavelength effective fields? Observe that the compact boson theory itself has various symmetries such as

$$\begin{aligned} U(1)_\theta : \theta &\mapsto \theta + \chi, \quad \mathbb{Z}_2^\theta : \theta \mapsto -\theta, \\ U(1)_\phi : \phi &\mapsto \phi + \xi, \quad \mathbb{Z}_2^\phi : \phi \mapsto -\phi, \end{aligned} \quad (11)$$

which form the group $G_{IR} \cong O(2)_\theta \times O(2)_\phi$ [43].

The action of symmetries can also be studied in the spectrum of local scaling operators $\mathcal{X}_{m,n} \equiv \exp(i(m\theta + n\phi))$ with scaling dimensions $[\mathcal{X}_{m,n}] = m^2 K_{\text{eff}} + \frac{n^2}{4K_{\text{eff}}}$ where m and n are integers. These read as follows:

$$\begin{aligned} U(1)_\theta : \mathcal{X}_{m,n} &\mapsto e^{im\chi} \mathcal{X}_{m,n}, \quad \mathbb{Z}_2^\theta : \mathcal{X}_{m,n} \mapsto \mathcal{X}_{-m,n}, \\ U(1)_\phi : \mathcal{X}_{m,n} &\mapsto e^{in\xi} \mathcal{X}_{m,n}, \quad \mathbb{Z}_2^\phi : \mathcal{X}_{m,n} \mapsto \mathcal{X}_{m,-n}. \end{aligned} \quad (12)$$

The question we are interested in is how the microscopic symmetries of spins G_{UV} listed in Table I attach themselves to those of compact boson degrees of freedom G_{IR} . In other words, we are interested in the *homomorphisms* $G_{UV} \rightarrow G_{IR}$. Distinct homomorphisms will lead to inequivalent symmetry-enriched Luttinger liquids that cannot be adiabatically connected. We will determine this for each phase one-by-one to confirm this.

1. Effective symmetries of XY_0

Let us begin with the gapless phase seen in the small- J limit XY_0 . The effective action of symmetries were already obtained using the bosonization formulas as listed in Table II. This can also be used to determine the action on various scaling operators as shown in Table III. We see that the

TABLE III. Effective action of symmetries in the XY_0 phase.

$U(1)$	\mathbb{Z}_2^R	\mathbb{Z}	\mathbb{Z}_2^P
$\begin{pmatrix} \theta(x) + \chi \\ \phi(x) \end{pmatrix}$	$\begin{pmatrix} -\theta(x) \\ -\phi(x) \end{pmatrix}$	$\begin{pmatrix} \theta(x) \\ \phi(x) \end{pmatrix}$	$\begin{pmatrix} \pi + \theta(-x) \\ -\phi(-x) \end{pmatrix}$
$e^{im\chi} \mathcal{X}_{m,n}(x)$	$\mathcal{X}_{-m,-n}(x)$	$\mathcal{X}_{m,n}(x)$	$e^{i\pi m} \mathcal{X}_{m,-n}(-x)$

microscopic $U(1)$ attaches itself to $U(1)_\theta$, \mathbb{Z}_2^R to a simultaneous action of \mathbb{Z}_2^θ and \mathbb{Z}_2^ϕ , and \mathbb{Z}_2^P to a composite action of simultaneous π rotation of $U(1)_\theta$ and \mathbb{Z}_2^ϕ action while UV lattice translations \mathbb{Z} have no effect in the IR.

2. Effective symmetries of XY_1 and XY_1^*

We now consider the gapless phases in the large- J limit obtained when $\mathcal{W}_- \equiv \cos(\theta_1 - \theta_2)$ dominates at long distances pinning $\vartheta \equiv \theta_1 - \theta_2$. To determine the nature of the resulting compact boson CFT the system flows to, we perform the following $SL(2, \mathbb{Z})$ transformation, which preserves the unit compactification radius of the fields as well as the canonical commutation relation Eq. (8),

$$\begin{pmatrix} \vartheta \\ \theta \end{pmatrix} \equiv \begin{pmatrix} \theta_1 - \theta_2 \\ \theta_2 \end{pmatrix}, \quad \begin{pmatrix} \varphi \\ \phi \end{pmatrix} \equiv \begin{pmatrix} \phi_1 \\ \phi_1 + \phi_2 \end{pmatrix}. \quad (13)$$

When $\vartheta \equiv \theta_1 - \theta_2$ is pinned, its conjugate φ is disordered and we obtain physics at long distances by setting

$$e^{im\vartheta} \approx \langle e^{im\vartheta} \rangle \approx e^{im\langle\vartheta\rangle} \text{ and } e^{in\varphi} \approx \langle e^{in\varphi} \rangle \approx 0. \quad (14)$$

The effective theory is simply that of the unpinned canonically conjugate pair of fields, $\theta = \theta_2$ and $\phi = \phi_1 + \phi_2$ with a Hamiltonian of the form shown in Eq. (10).

Using Eq. (14) and the action of the symmetries on the compact bosons obtained from bosonization at large J shown in Table II, we can read off the effective symmetry action on the θ and ϕ as well as on the spectrum of scaling operators as shown in Table IV. First, compare these with Table III. We see that the actions of $U(1)$ and \mathbb{Z}_2^R are identical in all three phases. However, the action of \mathbb{Z} distinguishes XY_0 from the other two. Finally, the symmetry action of \mathbb{Z}_2^P depends on the value of $\langle\vartheta\rangle$ and distinguishes between XY_1 ($\langle\vartheta\rangle = \pi$) and XY_1^* ($\langle\vartheta\rangle = 0$). Observe that both *electric* scaling operators [i.e., those carrying $U(1)$ charge] with the

 TABLE IV. Effective action of symmetries in the XY_1 ($\langle\vartheta\rangle = \pi$), and XY_1^* ($\langle\vartheta\rangle = 0$) phases.

$U(1)$	\mathbb{Z}_2^R	\mathbb{Z}	\mathbb{Z}_2^P
XY_1			
$\begin{pmatrix} \theta(x) + \chi \\ \phi(x) \end{pmatrix}$	$\begin{pmatrix} -\theta(x) \\ -\phi(x) \end{pmatrix}$	$\begin{pmatrix} \theta(x) + \pi \\ \phi(x) \end{pmatrix}$	$\begin{pmatrix} \theta(-x) + \pi \\ -\phi(-x) \end{pmatrix}$
$e^{im\chi} \mathcal{X}_{m,n}(x)$	$\mathcal{X}_{-m,-n}(x)$	$e^{i\pi m} \mathcal{X}_{m,n}(x)$	$e^{i\pi m} \mathcal{X}_{m,-n}(-x)$
XY_1^*			
$\begin{pmatrix} \theta(x) + \chi \\ \phi(x) \end{pmatrix}$	$\begin{pmatrix} -\theta(x) \\ -\phi(x) \end{pmatrix}$	$\begin{pmatrix} \theta(x) + \pi \\ \phi(x) \end{pmatrix}$	$\begin{pmatrix} \theta(-x) \\ -\phi(-x) \end{pmatrix}$
$e^{im\chi} \mathcal{X}_{m,n}(x)$	$\mathcal{X}_{-m,-n}(x)$	$e^{i\pi m} \mathcal{X}_{m,n}(x)$	$\mathcal{X}_{m,-n}(-x)$

 TABLE V. Effective action of symmetries in the XY_2 ($\langle\vartheta\rangle = 0$), and XY_2^* ($\langle\vartheta\rangle = \pi$) phases.

$U(1)$	\mathbb{Z}_2^R	\mathbb{Z}	\mathbb{Z}_2^P
XY_2			
$\begin{pmatrix} \theta(x) + 2\chi \\ \phi(x) \end{pmatrix}$	$\begin{pmatrix} -\theta(x) \\ -\phi(x) \end{pmatrix}$	$\begin{pmatrix} \theta(x) \\ \phi(x) + \pi \end{pmatrix}$	$\begin{pmatrix} \theta(-x) \\ \pi - \phi(-x) \end{pmatrix}$
$e^{2im\chi} \mathcal{X}_{m,n}(x)$	$\mathcal{X}_{-m,-n}(x)$	$e^{i\pi n} \mathcal{X}_{m,n}(x)$	$e^{i\pi n} \mathcal{X}_{m,-n}(-x)$
XY_2^*			
$\begin{pmatrix} \theta(x) + 2\chi \\ \phi(x) \end{pmatrix}$	$\begin{pmatrix} -\theta(x) \\ -\phi(x) \end{pmatrix}$	$\begin{pmatrix} \theta(x) \\ \phi(x) + \pi \end{pmatrix}$	$\begin{pmatrix} \theta(-x) \\ -\phi(-x) \end{pmatrix}$
$e^{2im\chi} \mathcal{X}_{m,n}(x)$	$\mathcal{X}_{-m,-n}(x)$	$e^{i\pi n} \mathcal{X}_{m,n}(x)$	$\mathcal{X}_{m,-n}(-x)$

smallest scaling dimensions, $\cos \theta$ and $\sin \theta$ are pseudoscalars for XY_1 and scalars in XY_1^* respectively. Thus, we have succeeded in establishing that XY_0 , XY_1 , and XY_1^* are distinct from each other.

3. Effective symmetries of XY_2 and XY_2^*

Finally, we turn to the large- J gapless phases obtained when \mathcal{V}_- dominates at long distances and pins $\phi_1 - \phi_2$. To get the effective symmetries of the resulting compact boson CFT the system flows to, we perform a different $SL(2, \mathbb{Z})$ transformation from Eq. (13),

$$\begin{pmatrix} \vartheta \\ \theta \end{pmatrix} \equiv \begin{pmatrix} \theta_1 \\ \theta_1 + \theta_2 \end{pmatrix}, \quad \begin{pmatrix} \varphi \\ \phi \end{pmatrix} \equiv \begin{pmatrix} \phi_1 - \phi_2 \\ \phi_2 \end{pmatrix}. \quad (15)$$

When $\varphi \equiv \phi_1 - \phi_2$ is pinned, its conjugate ϑ is disordered and we obtain the long distance physics by setting

$$e^{im\vartheta} \approx \langle e^{im\vartheta} \rangle \approx 0, \text{ and } e^{in\varphi} \approx \langle e^{in\varphi} \rangle \approx e^{in\langle\varphi\rangle}. \quad (16)$$

The effective theory is simply that of the unpinned fields θ and ϕ with an effective Hamiltonian of the form shown in Eq. (10).

Using Eq. (16) the symmetry action on the effective low-energy fields and on the spectrum of operators can be read off from Table II and is summarized in Table V. The most striking feature is that the θ field is a charge 2 operator for the $U(1)$ symmetry. Consequently, the smallest $U(1)$ charge carried by the spectrum of scaling operators is 2. This immediately shows that XY_2 and XY_2^* are distinct from XY_0 , XY_1 , and XY_1^* . Let us now focus on the effective action of \mathbb{Z}_2^P , which seemingly depends on the value of $\langle\varphi\rangle$ and distinguishes XY_2 from XY_2^* . This is *not* true—the symmetry actions are merely related by a change of basis. However, keeping track of other symmetry charges exposes the distinction. Consider magnetic scaling operators [those without any $U(1)$ charge] with the smallest scaling dimensions, $\cos \phi$ and $\sin \phi$. We see that in XY_2 , the operator with \mathbb{Z}_2^R charge ($\sin \phi$) transforms as a scalar under \mathbb{Z}_2^P whereas the operator without \mathbb{Z}_2^R charge ($\cos \phi$) transforms as a pseudoscalar. This situation is precisely reversed for XY_2^* where the \mathbb{Z}_2^R charged operator is a \mathbb{Z}_2^P pseudoscalar, whereas the \mathbb{Z}_2^R neutral operator is a \mathbb{Z}_2^P scalar. This completes the proof that the five gapless phases are distinct.

TABLE VI. Local and nonlocal order observables for large $|x - y|$. We denote algebraic and exponential decay by “alg” and “exp”.

	XY_0	XY_1	XY_1^*	XY_2	XY_2^*
$(O_s^+(x)O_s^-(y))$	alg	exp	alg	exp	exp
$(O_a^+(x)O_a^-(y))$	alg	alg	exp	exp	exp
$(C(x, y))$	0	0	0	0	$\neq 0$

4. Explicit symmetry breaking

Observe that all four microscopic symmetries were important in establishing these distinctions. Explicitly breaking certain symmetries eliminates the distinction between certain phases and opens a potential path to connect them without phase transitions or intermediate phases. Let us look at a few instances.

(1) If we break \mathbb{Z}_2^R , the distinction between XY_2 and XY_2^* is eliminated and reduces five phases to four, XY_0, XY_1, XY_1^* , and $(XY_2 = XY_2^*)$.

(2) If we break \mathbb{Z}_2^P , the distinction between XY_1 and XY_1^* is eliminated, as well as between XY_2 and XY_2^* and reduces the five phases to three, $XY_0, (XY_1 = XY_1^*),$ and $(XY_2 = XY_2^*)$.

(3) If we only preserve $U(1)$ and break all other symmetries, the five phases reduce to two, $(XY_0 = XY_1 = XY_1^*)$ and $(XY_2 = XY_2^*)$.

D. Local and nonlocal observables

We now turn to how we can physically characterize various gapless phases using local and nonlocal observables. We will use the previously determined effective symmetry action listed in Tables III to V to guide us in this. We will focus on two local operators O_s^\pm, O_a^\pm and a nonlocal string operator $C_{x,y}$ defined as follows [in both the small- J ($J_<$) and large- J ($J_>$) representations]:

$$O_s^\pm(j) \equiv \begin{cases} S_{2j-1}^\pm + S_{2j}^\pm & J_< \\ S_{1,j}^\pm + S_{2,j}^\pm & J_> \end{cases}, \quad (17)$$

$$O_a^\pm(j) \equiv \begin{cases} S_{2j-1}^\pm - S_{2j}^\pm & J_< \\ S_{1,j}^\pm - S_{2,j}^\pm & J_> \end{cases}, \quad (18)$$

$$C(j, k) \equiv \begin{cases} \sigma_{2j-1}^z (\prod_{l=2j}^{2k} \sigma_l^z) \sigma_{2k+1}^z & J_< \\ \sigma_{2,j}^z (\prod_{l=j+1}^{k-1} \sigma_{1,l}^z \sigma_{2,j}^z) \sigma_{1,k}^z & J_> \end{cases}. \quad (19)$$

The nature of two-point correlation functions of the local operators and the expectation value of the string operator are summarized in Table VI and completely characterize the phases. We see in Table VI that local operators uniquely identify the $XY_0, XY_1,$ and XY_2 phases but cannot distinguish between the XY_2 and XY_2^* phases, which the nonlocal operator can. In this section, we will see how this behavior can be determined using the bosonization formulas as well as using the effective symmetry action shown in Tables III to V. These predictions will also be confirmed numerically in Sec. V.

1. Local operator behavior from bosonization

Let us begin with XY_0 where, using Eq. (5) the local operators can be bosonized as

$$O_s^\pm(x) \sim e^{\pm i\theta(x)} \cos \phi(x), \quad O_a^\pm(x) \sim e^{\pm i\theta(x)}. \quad (20)$$

In Eq. (20), we have suppressed the bosonization prefactors and retained only the most relevant scaling operators the lattice operators have an overlap with. Clearly, the two-point functions of O_s^\pm and O_a^\pm are expected to have algebraic decay governed by the parameters of the effective compact-boson CFT that describe the phase at long distances. Recall that for a CFT, the correlation functions of the scaling operators $\mathcal{X}(x)$ with scaling dimensions $\Delta_{\mathcal{X}}$ scale as

$$\langle \mathcal{X}(x)\mathcal{X}^\dagger(y) \rangle \sim |x - y|^{-2\Delta_{\mathcal{X}}}. \quad (21)$$

Thus, at long distances $|x - y|$, we expect

$$\begin{aligned} |\langle O_s^+(x)O_s^-(y) \rangle| &\sim |x - y|^{-(2K + \frac{1}{2K})}, \\ |\langle O_a^+(x)O_a^-(y) \rangle| &\sim |x - y|^{-\frac{1}{2K}}. \end{aligned} \quad (22)$$

Let us now consider the large- J phases where, using Eq. (9), we get

$$\begin{aligned} O_s^\pm(x) &\sim (e^{\pm i\theta_1(x)} + e^{\pm i\theta_2(x)}), \\ O_a^\pm(x) &\sim (e^{\pm i\theta_1(x)} - e^{\pm i\theta_2(x)}). \end{aligned} \quad (23)$$

We have again suppressed bosonization prefactors and retained only the most relevant scaling operators. When we have the full $c = 2$ theory along the $t = 0$ line shown in Fig. 15 (see below) we see that both local operators have algebraic correlations. However, for $t \neq 0$, when \mathcal{V}_- or \mathcal{W}_- are relevant resulting in the different gapless phases, this changes. Consider the case where \mathcal{W}_- is the most relevant operator and pins $\vartheta \equiv \theta_1 - \theta_2$. We can use the $SL(2, \mathbb{Z})$ transformation shown in Eq. (13) and Eq. (14) to obtain the following:

$$\begin{aligned} O_s^\pm(x) &\sim (e^{\pm i\theta_1} + e^{\pm i\theta_2}) \approx e^{\pm i\theta} (1 + e^{\pm i(\vartheta)}) \\ &\approx \begin{cases} 0 & \text{for } \langle \vartheta \rangle = \pi (XY_1) \\ e^{\pm i\theta} & \text{for } \langle \vartheta \rangle = 0 (XY_1^*) \end{cases}, \\ O_a^\pm(x) &\sim (e^{\pm i\theta_1} - e^{\pm i\theta_2}) \approx e^{\pm i\theta} (1 - e^{\pm i(\vartheta)}) \\ &\approx \begin{cases} e^{\pm i\theta} & \text{for } \langle \vartheta \rangle = \pi (XY_1) \\ 0 & \text{for } \langle \vartheta \rangle = 0 (XY_1^*) \end{cases}. \end{aligned} \quad (24)$$

We see that for each case $\langle \vartheta \rangle = \pi/0$, only one of the two operators $O_s^\pm(x)/O_a^\pm(x)$ has vanishing overlap with scaling operators and has algebraic correlations whereas the other has exponential correlations,

$$\begin{aligned} |\langle O_s^+(x)O_s^-(y) \rangle| &\sim \begin{cases} e^{-\frac{|x-y|}{\xi}} & (XY_1) \\ |x - y|^{-\frac{1}{2K_{\text{eff}}}} & (XY_1^*) \end{cases}, \\ |\langle O_a^+(x)O_a^-(y) \rangle| &\sim \begin{cases} |x - y|^{-\frac{1}{2K_{\text{eff}}}} & (XY_1) \\ e^{-\frac{|x-y|}{\xi}} & (XY_1^*) \end{cases}. \end{aligned} \quad (25)$$

K_{eff} is the effective Luttinger parameter shown in Eq. (10) that characterizes the effective compact boson CFT at long distances. We may wonder if the calculations above are modified if we include the corrections to the bosonization formulas represented by ellipses in Eq. (9). It turns out that the answer is no and can be verified by including all higher terms explicitly. A more powerful way is using symmetries, as will be discussed in the next subsection.

We now turn to the phases obtained when \mathcal{V}_- is dominant and pins $\varphi \equiv \phi_1 - \phi_2$. Using the $SL(2, \mathbb{Z})$ transformation

TABLE VII. Symmetries transformations of local and nonlocal operators defined in Eqs. (17) to (19).

	$O_s^\pm(x) \mapsto$	$O_a^\pm(x) \mapsto$	$C(x, y) \mapsto$
$U(1)$	$e^{\pm i x} O_s^\pm(x)$	$e^{\pm i x} O_a^\pm(x)$	$C(x, y)$
\mathbb{Z}_2^R	$O_s^\mp(x)$	$O_a^\mp(x)$	$C(x, y)$
\mathbb{Z}_2^P	$O_s^\pm(-x)$	$-O_a^\pm(-x)$	$C(-y, -x)$

shown in Eq. (15) as well as Eq. (16), we get

$$\begin{aligned} O_s^\pm &\sim e^{\pm i\theta_1} + e^{\pm i\theta_2} \approx ((e^{\pm i\vartheta}) + e^{\pm i\theta} \langle e^{\mp i\vartheta} \rangle) \approx 0, \\ O_a^\pm &\sim e^{\pm i\theta_1} - e^{\pm i\theta_2} \approx ((e^{\pm i\vartheta}) - e^{\pm i\theta} \langle e^{\mp i\vartheta} \rangle) \approx 0. \end{aligned} \quad (26)$$

We see that both $O_s^\pm(x)$ and $O_a^\pm(x)$ have no overlap with any scaling functions and therefore their correlation functions decay exponentially

$$|\langle O_s^+(x) O_s^-(y) \rangle| \sim |\langle O_a^+(x) O_a^-(y) \rangle| \sim e^{-\frac{|x-y|}{\xi}}. \quad (27)$$

We can check that this behavior does not change even when corrections represented by ellipses in Eq. (9) are included. This can also be justified using symmetry arguments as we will now see.

2. Local operator behavior from effective symmetry action

The correlations of local operators shown in Table VI can also be understood directly by using symmetries. Let us begin by noting down the transformations of the local operators under the $U(1)$, \mathbb{Z}_2^R and \mathbb{Z}_2^P symmetries. This is shown in Table VII. At this point, let us remark that all local operators are charged under various internal symmetries. The nonlocal operator, on the other hand, although is neutral overall, has end points that carry \mathbb{Z}_2^R charge. This is important to establish the topological nature of phases and will be discussed in Sec. IV. Now, we can ask if the transformations shown in Table VII can be obtained in each of the five gapless phases using combinations of the scaling operators $\mathcal{X}_{mn}(x)$ whose transformations are shown in Tables III to V. If the answer is yes, it will mean that the local operator will have algebraic correlations at long distances with the exponent determined by the scaling dimensions of the said operators with smallest scaling dimensions. If not, then the operators will have exponentially decaying correlations

XY_0 : Comparing the $U(1)$ transformations shown in Table VII and Table III tells us that O_s^\pm and O_a^\pm can have overlap with $\mathcal{X}_{\pm 1, n}$. Comparing the \mathbb{Z}_2^P action tells us that the smallest operators that transform correctly are

$$O_s^\pm(x) \sim \mathcal{X}_{\pm 1, 1} + \mathcal{X}_{\pm 1, -1} \sim e^{\pm i\theta} \cos \phi, \quad (28)$$

$$O_a^\pm(x) \sim \mathcal{X}_{\pm 1, 0} \sim e^{\pm i\theta}, \quad (29)$$

which is precisely what was obtained from the bosonization formulas in Eq. (20) and Eq. (22). This combination also transforms correctly under \mathbb{Z}_2^R .

XY_1 and XY_1^* : Comparing the $U(1)$ transformations shown in Table VII and Table IV again tells us that O_s^\pm and O_a^\pm can overlap with $\mathcal{X}_{\pm 1, n}$. It is easy to check that no combination of scaling operators $\mathcal{X}_{\pm 1, n}$ can simultaneously reproduce the \mathbb{Z}_2^P and \mathbb{Z}_2^R transformations of $O_s^\pm(x)$ (for $\langle \vartheta \rangle = \pi$, that is,

XY_1) and $O_a^\pm(x)$ (for $\langle \vartheta \rangle = 0$, that is, XY_1^*) and therefore have correlations that decay exponentially. On the other hand, $\mathcal{X}_{\pm 1, 0} \sim e^{\pm i\theta}$ has the right transformation properties as $O_a^\pm(x)$ (for $\langle \vartheta \rangle = \pi$, i.e., XY_1) and $O_s^\pm(x)$ (for $\langle \vartheta \rangle = 0$, i.e., XY_1^*). This reproduces Eqs. (24) and (25).

XY_2 and XY_2^* : The effective $U(1)$ transformations in Table V tell us that all scaling operators have a minimum $U(1)$ charge of 2 and therefore there are no combinations of scaling operators that have the transformation properties of O_s^\pm and O_a^\pm and that have a unit $U(1)$ charge as seen in Table VII. Consequently, the correlations of O_s^\pm and O_a^\pm have exponential decay in both XY_2 and XY_2^* phases [44]. This reproduces Eqs. (26) and (27).

3. Behavior of the nonlocal operator

We now turn to the nonlocal string operator $C(x, y)$ defined in Eq. (19), which can be bosonized in both the small- J ($J_<$) and large- J ($J_>$) limits as follows (see Appendix C for details):

$$C(x, y) \sim C_L(x) C_R(y), \quad (30)$$

$$C_{L/R} \approx \begin{cases} \gamma \sin\left(\frac{\phi}{2}\right) & (J_<) \\ \alpha \sin\left(\frac{\phi_1 + \phi_2}{2}\right) + \beta \sin\left(\frac{\phi_1 - \phi_2}{2}\right) & (J_>), \end{cases} \quad (31)$$

where we have only shown operators with the smallest scaling dimensions and α, β, γ are nonzero coefficients whose values we do not fix. It is now easy to verify how $\langle C(x, y) \rangle$ behaves at large $|x - y|$. From Eq. (30), we have

$$\langle C(x, y) \rangle \sim \langle C_L(x) \rangle \langle C_R(y) \rangle. \quad (32)$$

Therefore, when $\langle C_{L/R} \rangle \neq 0$, we have $\langle C(x, y) \rangle \neq 0$. Among the phases without spontaneous symmetry breaking, this happens when $\langle \phi \rangle = \pi$ for small J and $\langle \phi_1 \pm \phi_2 \rangle = \pi$ for large J . From Figs. 14 and 15 (see below), we see that $\langle C(x, y) \rangle \neq 0$ in the Haldane and XY_2^* phases whereas in the trivial gapped phase and other gapless phases XY_0, XY_1 , and XY_1^* , $C(x, y) \rightarrow 0$ for sufficiently large $|x - y|$. This confirms the remaining entries of Table VI.

IV. BOSONIZATION ANALYSIS II: THE TOPOLOGICAL NATURE OF XY_2^*

We now focus on the XY_2^* gapless phase and study its topological nature. First, we show that it has protected edge modes and then discuss the nature of the topological phase. In particular, we show that the gapless topological phase is not ‘‘intrinsically gapless’’ and briefly discuss a related model where it is.

A. Edge modes

A hallmark of gapped symmetry-protected topological phases such as topological insulators and superconductors is the presence of protected edge modes degenerate with the ground state, which have exponentially small splitting at finite system sizes. Gapless topological phases are defined as those that have edge modes protected by symmetries and can be sharply identified at finite volumes by exponential or algebraic splitting with coefficients different from bulk states [14–17, 19]. Recall that XY_2^* was characterized by a nonzero expectation value of the string operator $C(x, y)$ whose

endpoints were charged under \mathbb{Z}_2^R . The following argument presented in [18,19] shows that this automatically implies the presence of edge modes. Let us first present the argument using lattice operators and then using bosonization.

1. Argument using lattice operators

Let $|\psi\rangle$ be the ground state of the XY_2^* Luttinger liquid, which has string order

$$\langle\psi|C(x,y)|\psi\rangle \neq 0. \quad (33)$$

We also know that $|\psi\rangle$ is invariant under the symmetries shown in Table I. Let us consider $U(1)$ rotation by angle $\chi = \pi$ generated by the following operator (we only consider the large- J notation for convenience):

$$U(\pi) \propto \prod_{j=1}^L (\sigma_{j,1}^z \sigma_{j,2}^z), \quad U(\pi)|\psi\rangle \propto |\psi\rangle. \quad (34)$$

This operator acts on a finite chain of length L with unit cells labeled $j = 0, \dots, L$. Let us now consider the action of the string operator defined on the full length of the chain, i.e.,

$$C(0, L) \equiv \sigma_{0,2}^z \left(\prod_{j=2}^{L-1} \sigma_{j,1}^z \sigma_{j,2}^z \right) \sigma_{L,1}^z. \quad (35)$$

We use this along with $U(\pi)$ to get the following result:

$$\begin{aligned} \langle\psi|C(x,y)|\psi\rangle \neq 0 &\Rightarrow \langle\psi|C(x,y)U(\pi)|\psi\rangle \neq 0 \\ &\Rightarrow \langle\psi|\sigma_{1,1}^z \sigma_{L,2}^z|\psi\rangle \neq 0. \end{aligned} \quad (36)$$

By cluster decomposition, we have

$$\langle\psi|\sigma_{1,1}^z|\psi\rangle \neq 0 \quad \text{and} \quad \langle\psi|\sigma_{L,2}^z|\psi\rangle \neq 0. \quad (37)$$

This proves that when we have string order, we also have edge magnetization. Since $\sigma_{1,1}^z$ and $\sigma_{L,2}^z$ are charged under symmetry \mathbb{Z}_2^R , we can interpret this result as spontaneously breaking the symmetry at the edges and resulting in degenerate edge modes.

2. Argument using bosonization

It is nice to obtain the same result using bosonization. Let us first write down the bosonized version of $U(\pi)$ (see Appendix C),

$$U(\pi) \sim U_L(\pi)U_R(\pi), \quad (38)$$

$$U_{L/R} \approx \begin{cases} \cos\left(\frac{\phi}{2}\right) & (J_<) \\ \gamma \cos\left(\frac{\phi_1+\phi_2}{2}\right) + \delta \cos\left(\frac{\phi_1-\phi_2}{2}\right) & (J_>). \end{cases} \quad (39)$$

In the phases with $\langle C(x,y) \rangle \neq 0$, letting the string operator span the length of the system setting $x = 0$, $y = L$ we have

$$\langle C(0, L)U(\pi) \rangle = \langle C_L U_L \rangle_{x=0} \langle C_R U_R \rangle_{x=L} \neq 0. \quad (40)$$

By cluster-decomposition, we get

$$\langle C_{L/R} U_{L/R}(\pi) \rangle \neq 0. \quad (41)$$

Using Eqs. (31) and (39), this reduces to

$$\begin{aligned} C_{L/R} U_{L/R}(\pi) &\sim \sin \phi + \dots \quad \text{for small } J, \\ C_{L/R} U_{L/R}(\pi) &\sim \tilde{\alpha} \sin \phi_1 + \tilde{\beta} \sin \phi_2 + \tilde{\gamma} \sin(\phi_1 + \phi_2) \\ &\quad + \tilde{\delta} \sin(\phi_1 - \phi_2) + \dots \quad \text{for large } J. \end{aligned}$$

$\tilde{\alpha}, \dots, \tilde{\delta}$ are some constants whose precise values are irrelevant. We see that $C_{L/R} U_{L/R}(\pi)$ are proper local operators (without fractional coefficients) carrying \mathbb{Z}_2^R charge. Therefore, we have spontaneous symmetry breaking at the edges and associated boundary degeneracy whenever we have $\langle C(x,y) \rangle \neq 0$ and unbroken $U(\pi)$ symmetry, such as the Haldane and XY_2^* phases.

B. Why XY_2^* is not an intrinsically gapless topological phase?

In the taxonomy of gapless topological phases [14–17,19], a special role is played by so-called intrinsically gapless topological phases [19,45,46]. These are gapless phases with stable edge modes protected by symmetries that do not allow gapped topological phases. In this sense, the topological nature is intrinsically gapless. Phase diagrams in which intrinsically gapless topological phases can be found cannot, by definition, contain gapped topological phases. Therefore, the phase diagrams shown in Fig. 2 that contain the Haldane phase, which is a gapped topological phase, make it clear that the XY_2^* phase is not intrinsically gapless. This is because the symmetries of the model $G \cong O(2) \times \mathbb{Z}_2^P \times \mathbb{Z}$ protect both gapless and gapped topological phases. We can ask whether we can break certain symmetries to preserve only the gapless topological phase but eliminate the gapped one. We now show using bosonization that this too is not possible.

Let us focus on the large- J limit where XY_2^* is present. From Fig. 15 (see below), we see that the gapped Haldane phase is obtained when $\langle \phi_1 + \phi_2 \rangle = \pi$ whereas the XY_2^* obtains when $\langle \phi_1 - \phi_2 \rangle = \pi$. Let us consider the possibility of eliminating the Haldane phase that has a gap while preserving XY_2^* by adding an operator that ensures that $\langle \phi_1 + \phi_2 \rangle$ can be tuned smoothly to zero, while $\langle \phi_1 - \phi_2 \rangle$ can only be pinned to 0 or π . The operator that achieves this is

$$\delta H \sim \int dx \sin(\phi_1 + \phi_2). \quad (42)$$

However, note that the addition of Eq. (42) simultaneously breaks both \mathbb{Z}_2^R and \mathbb{Z}_2^P symmetries. Therefore, any lattice operator that produces Eq. (42) also generically produces an operator of the form

$$\delta H' \sim \int dx \sin(\phi_1 - \phi_2), \quad (43)$$

which smoothly tunes the pinned value of $\langle \phi_1 + \phi_2 \rangle$ to zero and therefore eliminates XY_2^* [47].

C. A related model where XY_2^* is an intrinsically gapless topological phase

We now present a model where XY_2^* is an intrinsically gapless topological phase. We work in the large- J limit and modify the Hamiltonian in Eq. (2) as shown in Fig. 3 by

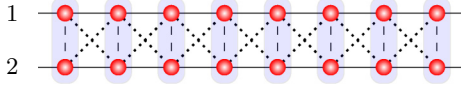


FIG. 3. Schematic representation of the Hamiltonian in Eq. (44), which can host an intrinsically gapless SPT.

adding an extra term as follows:

$$\begin{aligned}
 H &= H_1 + H_2 + H_\perp + H'_\perp + H''_\perp, \text{ where,} \\
 H_\alpha &= J \sum_j (S_{\alpha j}^x S_{\alpha j+1}^x + S_{\alpha j}^y S_{\alpha j+1}^y - \Delta S_{\alpha j}^z S_{\alpha j+1}^z), \\
 H_\perp &= (1-t) \sum_j (S_{1j}^x S_{2j}^x + S_{1j}^y S_{2j}^y - \lambda S_{1j}^z S_{2j}^z), \\
 H'_\perp &= \frac{(1+t)}{2} \sum_j (S_{2j}^x S_{1j+1}^x + S_{2j}^y S_{1j+1}^y - \lambda S_{2j}^z S_{1j+1}^z), \\
 H''_\perp &= \frac{(1+t)}{2} \sum_j (S_{1j}^x S_{2j+1}^x + S_{1j}^y S_{2j+1}^y - \lambda S_{1j}^z S_{2j+1}^z). \quad (44)
 \end{aligned}$$

The presence of the new term H''_\perp preserves all original symmetries shown in Table I but importantly introduces a new on-site symmetry, which exchanges the two legs. The action on spin operators and large- J bosonized variables is as follows:

$$\mathbb{Z}_2^L : \tilde{S}_{1,j} \leftrightarrow \tilde{S}_{2,j}, \phi_1 \leftrightarrow \phi_2, \theta_1 \leftrightarrow \theta_2. \quad (45)$$

Remarkably, the bosonized version of Eq. (44) is identical to Eq. (9) and therefore should contain the same phases although in different parameter regimes. Let us now consider including lattice operators that explicitly break the \mathbb{Z}_2^R and \mathbb{Z}_2^L symmetries but preserve the new \mathbb{Z}_2^L symmetry shown in Eq. (45). In the continuum limit, this introduces only the perturbation shown in Eq. (42) but not Eq. (43) since the latter breaks \mathbb{Z}_2^L . As explained above, this eliminates the Haldane phase. The equivalent of XY_2^* phase in this model is an intrinsically gapless topological phase. Indeed, the residual on-site unitary symmetry $U(1) \times \mathbb{Z}_2^L$ is known to not host any gapped symmetry-protected topological phases in one dimension [48]. We leave the numerical study of the model in Eq. (44) to future work.

V. NUMERICAL ANALYSIS

In this section, we numerically analyze the system at hand and validate the analytical results predicted above. We map the spin system to hardcore bosons, where the on-site occupancy is restricted to $n = 0/1$. The Hamiltonian in terms of hardcore bosons [see Eq. (2)] becomes

$$\begin{aligned}
 H_\alpha &= J \left[\sum_j \frac{1}{2} (b_{\alpha,j}^\dagger b_{\alpha,j+1} + \text{H.c.}) \right. \\
 &\quad \left. - \Delta (\tilde{n}_{\alpha,j} \tilde{n}_{\alpha,j+1}) \right], \quad \alpha = 1, 2,
 \end{aligned}$$

$$\begin{aligned}
 H_\perp &= (1-t) \left[\sum_j \frac{1}{2} (b_{1,j}^\dagger b_{2,j} + \text{H.c.}) - \lambda (\tilde{n}_{1,j} \tilde{n}_{2,j}) \right], \\
 H'_\perp &= (1+t) \left[\sum_j \frac{1}{2} (b_{2,j}^\dagger b_{1,j+1} + \text{H.c.}) - \lambda (\tilde{n}_{2,j} \tilde{n}_{1,j+1}) \right], \quad (46)
 \end{aligned}$$

where b_j (b_j^\dagger) annihilation (creation) operators and $\tilde{n}_j = (n_j - \frac{1}{2})$ with n_j being the number operator for site j . The ground state of the model Hamiltonian is computed using the density matrix renormalization group (DMRG) method [49–51]. The bond dimension is taken to be ~ 500 , which is sufficient for convergence for typical system sizes $L = 200$ where L is the total number of sites in the system. Unless otherwise stated, sites are labeled using a single-site label convention of Eq. (1).

A. Diagnostics, phases, and phase transitions

We explore the parameter space in the $\lambda - t$ plane with fixed J and identify the phases and their transitions. The most illustrative limit is to first investigate when $J = 0$ [52] where the system, in the absence of any dimerization ($t = 0$), undergoes a first-order phase transition at $\lambda = 1$ [see Fig. 4(a)]. t engineers gapped phases between $0 < \lambda < \frac{1}{\sqrt{2}}$; however $t < 0$ is trivial and $t > 0$ is topological (Haldane phase) in nature. A gapless phase (XY_0) opens between $\frac{1}{\sqrt{2}} < \lambda < 1$ where both perturbations λ and t are irrelevant. Introducing a small finite J , not unexpectedly, only renormalizes the phase boundaries [see $J = 0.1$ $\lambda - t$ phase diagram in Fig. 4(b)] reducing the size of the gapless XY_0 phase. A further increase in J_2 leads to the emergence of two new gapless phases (XY_1) and XY_1^* as XY_0 disappears [see Fig. 4(c)] and we get the large- J picture.

To explore the large- J phase diagram schematically shown in Fig. 2, a particularly illustrative parameter choice is to explore the phase diagram for fixed $J = 2.5$ as shown in Fig. 5 ($\Delta = 0.1$). Four *distinct* symmetry-enriched critical phases are clearly obtained. To conclusively characterize the phase boundaries and the nature of their transitions, we use a host of diagnostics, which we now discuss.

1. BKT transitions

Transitions from the trivial gapped phase to XY_1 and the Haldane phase to XY_1^* belong to the BKT universality class. To characterize these transitions, it is useful to note that in the (hardcore) bosonic language, the XY_1 and XY_1^* phases are $\pi/2$ -superfluids [SF($\pi/2$)] phases [53,54]. In such systems, the momentum distribution is given by

$$N(k) = \frac{1}{L} \sum_{i,j} e^{ik|i-j|} \Gamma_{i,j}, \quad (47)$$

(where $\Gamma_{i,j} = \langle b_i^\dagger b_j \rangle$) and is expected to show a sharp peak at $k = \pi/2$. At the transition itself, the finite-size scaling of $N(\pi/2)$ carries the signature of an underlying BKT transition. For example, at the critical point, the BKT ansatz predicts $N(k) \propto L^{1-\frac{1}{2K}}$, which can be used to extract the value of K [55,56]. The perfect crossing of the $N(k = \pi/2)$ data for

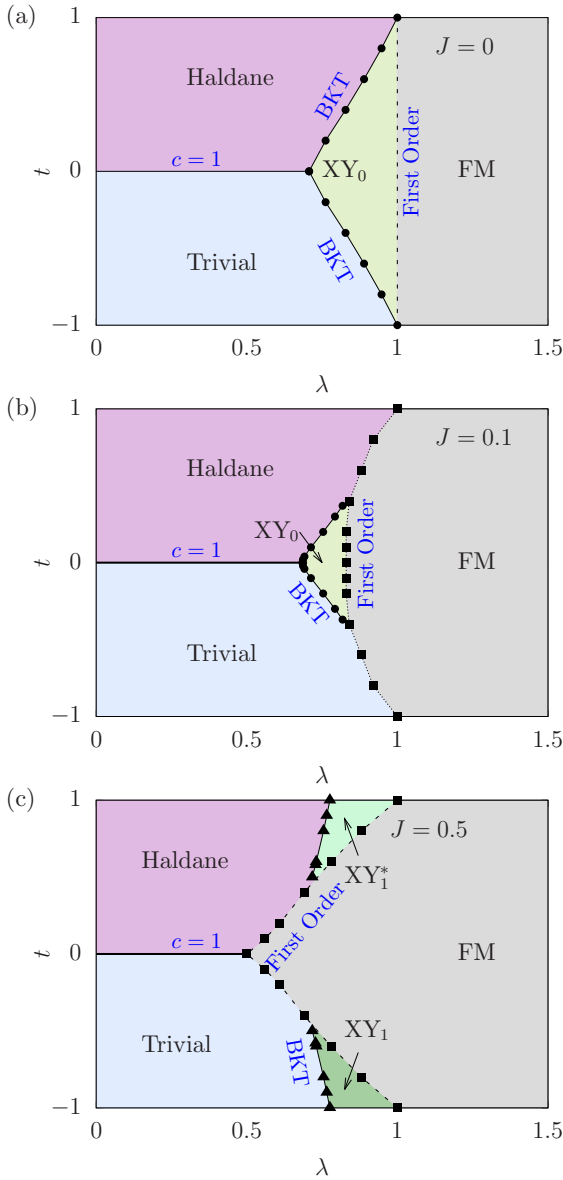


FIG. 4. Phase diagram for small J evaluated using DMRG corresponding to Hamiltonian [see Eq. (46)] for (a) $J = 0.0$, (b) $J = 0.1$, and (c) $J = 0.5$ $\Delta = \lambda$ in (a)–(c). Phase boundaries represent the second- and first-order transitions calculated using various diagnostics as mentioned in the text. The transition between the gapped, i.e., trivial, Haldane, and gapless, i.e., XY_0 , XY_1 , and XY_1^* , when they exist are BKT transitions and correspond to a single-component compact boson theory with central charge $c = 1$ and Luttinger parameter $K = 2$ whereas the transition between the Haldane and trivial phase is a single-component compact boson theory with central charge $c = 1$ and varying K . All transitions to the FM are first order. Symbols are the only calculated points, and lines connect the points for clarity.

different lengths at $t = -0.8$ as shown in Fig. 6(a) indicates a BKT transition, which has the Luttinger parameter of value $K = 2$ as expected from Sec. III (see also Appendix A). This is found to be true for all values of t using which the phase boundaries to the $SF(\pi/2)$ (XY_1) phase of Fig. 5 have been obtained.

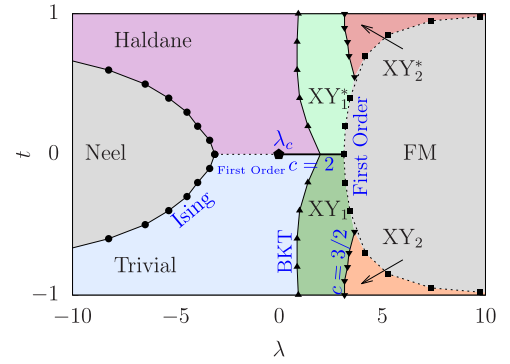


FIG. 5. Phase diagram for large J in $\lambda - t$ plane with fixed $J = 2.5$ and $\Delta = 0.1$. Bold circles mark the Ising transition with central charge $c = \frac{1}{2}$ between Néel to trivial and Néel to Haldane phase. The transition between trivial to XY_1 and Haldane to XY_1^* (up triangles) are BKT transitions, described by a single-component compact boson theory with $c = 1$ and Luttinger parameter $K = 2$. The transition from XY_1 to XY_1^* is a two-component compact boson theory with $c = 2$ with varying Luttinger parameters. The trivial-to-Haldane phase transition through the MG points is first order, which changes to $c = 2$ for larger λ at λ_c (pentagonal point). The transition from XY_1 to XY_2 and from XY_1^* to XY_2^* (down triangles) belong to the Ising universality class stacked on top of a compact boson with $c = \frac{3}{2}$. Finally, the transition from any phase to the FM phase is a first-order transition (squares). Note that symbols are the only calculated points, and lines connect the points for clarity.

2. Ising transitions

The transitions from the Néel to trivial and Haldane (circles), from XY_1 to XY_2 , and from XY_1^* to XY_2^* phase are found to be of Ising type (see Fig. 5). Such Ising transitions can be characterized by analyzing the finite-size scaling of the structure factor $S(k)$ defined by

$$S(k) = \frac{1}{L^2} \sum_{l,m} e^{ik(l-m)} (\langle n_l n_m \rangle - \langle n_l \rangle \langle n_m \rangle). \quad (48)$$

In the Néel state, $S(k)$ shows a peak at $k = \pi$ signaling antiferromagnetic correlations. At the Ising transitions, it is known that $S(k = \pi)$ follows a scaling ansatz $\propto L^{-\frac{2\beta}{\nu}}$ such that at the critical point $S(k)L^{\frac{2\beta}{\nu}}$ is invariant for different L with exponents $\nu = 1$ and $\beta = 1/8$ [57,58]. The perfect crossing of $S(k)L^{\frac{1}{4}}$ as shown in Fig. 6(b), and eventual collapse of all the data points, shown in Fig. 6(c), for different L in $S(\pi)L^{\frac{2\beta}{\nu}}$ vs $(\lambda - \lambda_c)L^\nu$ plane near the transition point implies an Ising phase transition at $t = -0.4$ with a critical point $\lambda_c \sim -5.41$. We use the same approach to calculate the Ising phase boundaries in the phase diagram (Fig. 5).

3. $c = \frac{3}{2}$ transition between gapless phases

Unlike the previous Ising transitions where one transits from a gapless to a gapped phase, the Ising transitions that appear between XY_1 to XY_2 and XY_1^* to XY_2^* are gapless-to-gapless transitions. Since this CFT appears in addition to the existing compact boson, the total central charge of the transition is expected to be $c = \frac{3}{2}$. Phase transition points are

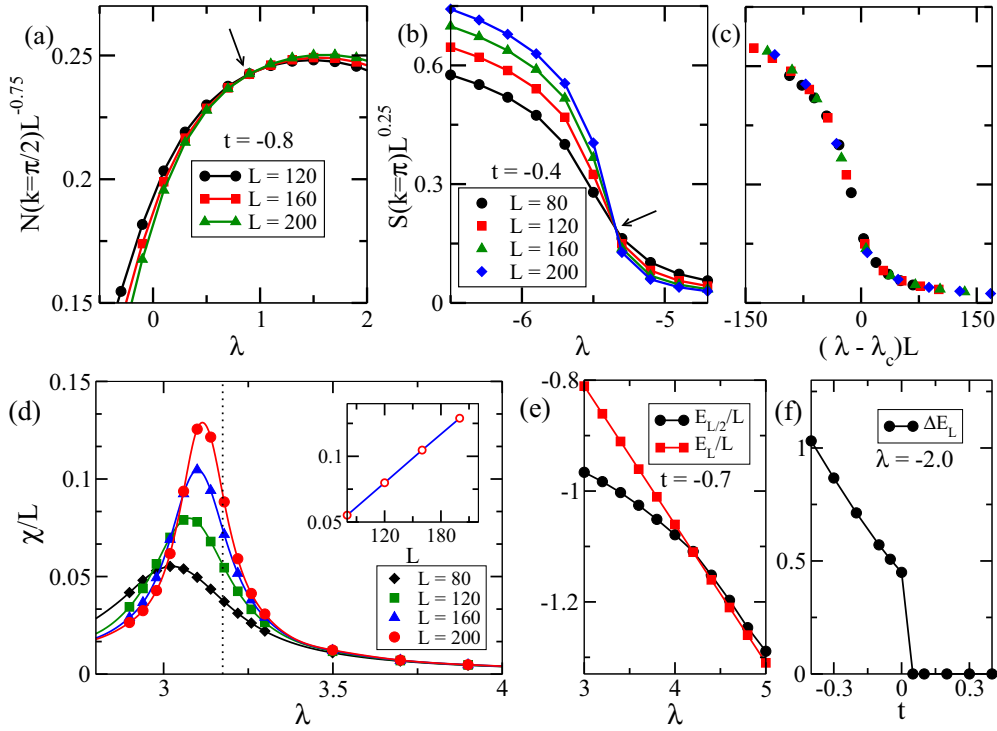


FIG. 6. The top row demonstrates the finite-size calling to determine (a) the BKT transition between the trivial and XY_1 phase and [(b),(c)] the Ising transition between the Néel and trivial phase. The perfect crossing of different $N(\pi/2)L^{\frac{2\beta}{\nu}-1}$ curves in (a) with $t = -0.8$ for different L implies the transition point with the Luttinger parameter $K = 2$ for the BKT transition. The crossing of different $S(\pi)L^{\frac{2\beta}{\nu}}$ curves with $t = -0.4$ for different L in (b) reveals the transition point with exponents $\nu = 1$ and $\beta = 1/8$. The collapse of all the data points for different L in $S(\pi)L^{\frac{2\beta}{\nu}}$ vs $(\lambda - \lambda_c)L^\nu$ shown in (c) further confirms the Ising transition point at $\lambda_c \sim -5.34$. The Ising transition between two gapless phases, from XY_1 to XY_2 phase, at $t = -1$ using the finite-size scaling of fidelity susceptibility (χ) shown in (d). The χ peaks at the transition point, and for the Ising transition, the peak height diverges linearly with L (inset). The transition point at the thermodynamic limit (dotted line) is calculated by extrapolating the peak positions for different L . The eigenvalues are plotted to determine the first-order transitions. (e) The level crossing in the ground-state energies E_N at $t = -0.7$ with $N = L/2$ and $N = L$ implies the first-order transition between the XY_2 and FM phase. (f) The sharp jump in single-particle excitation gap (ΔE_L with $\Delta n = 1$) at $t = 0$ for $\lambda = -2.0$ signifies the first-order transition between the trivial and Haldane phases. See the phase diagram in Fig. 5. In (e) and (f), we consider $L = 200$.

quantified by analyzing fidelity susceptibility (χ),

$$\chi = \lim_{(\lambda-\lambda') \rightarrow 0} \frac{-2\ln|\langle \psi(\lambda) | \psi(\lambda') \rangle|}{(\lambda - \lambda')^2} \quad (49)$$

where $|\psi(\lambda)\rangle$ is the ground state at λ . At the phase transition point, χ/L develops a peak, and the height of the peak diverges linearly with L for the Ising transition [59–61]. In Fig. 6(d), we plot χ/L for different system sizes, which shows an increase in the peak height with L . The inset of Fig. 6(d) shows the linear divergence of the peak height, implying the Ising transition. The critical point of the transition is determined by extrapolating the position of the peak to the thermodynamic limit, which is marked by the dashed line in Fig. 6(d).

4. Multiversality along the $t = 0$ line

On $t = 0$ line, the gapless phase with $c = 2$ starts at $\lambda_c \sim -0.01$, which is a BKT transition point that can be calculated using finite-size scaling of single particle excitation gap [57]. The excitation gap at half-filling can be defined as

$$\Delta E_L = (E_{N-\Delta n} + E_{N+\Delta n} - 2E_N)/\Delta n, \quad (50)$$

where $N = L/2$ and Δn is the number of particles in an excitation. The invariance of $L\Delta E'_L$ with $\Delta n = 1$ at the critical point and the collapse of all the data in $L\Delta E'_L$ vs $x_{\lambda,L}$ plane, where

$$\begin{aligned} \Delta E'_L &= \Delta E_L [1 + 1/(2\ln L + C)], \\ x_{\lambda,L} &= \ln L - a/\sqrt{\lambda - \lambda_c}, \end{aligned} \quad (51)$$

at and near the critical point with a suitable choice of constants C and a predicts the BKT transition point $\lambda_c \sim -0.01$ (see Fig. 7 below).

From Fig. 5, we see that the $c = 2$ line separates the gapless phases XY_1 and XY_1^* as well as the trivial and Haldane gapped phases. The latter phases are separated by a different universality class with $c = 1$ for small J . This is a numerical confirmation of the “multiversality” [22,23] phenomenon discussed in Sec. III and Appendix A.

5. First-order transitions

Finally, the transition between the trivial and the Haldane gapped phase for negative values of λ at large J , or that between any of the phases to FM is first order in nature. These can be characterized by analyzing the level crossings between

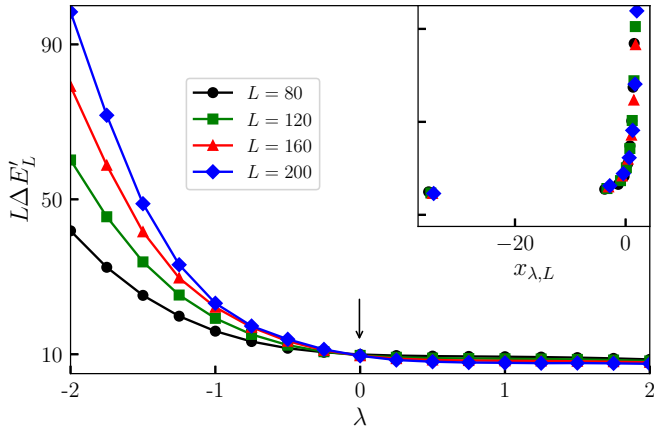


FIG. 7. Finite-size scaling of ΔE_L is shown to find the BKT transition point along $t = 0$ line for large J where the universality class changes from first order to second order with $c = 2$. The crossing of all curves captures the critical point, marked by the arrow. (Inset) The collapse of all the data for different L complements the BKT transition with $\lambda_c = -0.01$.

eigenstate energies. For instance, in the case of transitions to the FM phase, we plot the ground-state energy at boson half-filling ($E_{L/2}$), which corresponds to zero magnetization sector, and completely filled (E_L), which is equivalent to fully magnetized case (FM phase) across the boundary in Fig. 6(e). The crossing between $E_{L/2}$ and E_L determines the first-order transition points, which are marked by squares in the phase diagram (Fig. 5). On the other hand, the sharp jump in single particle excitation gap ΔE_L [Eq. (50) with $\Delta n = 1$] at $t = 0$ for the transition between the trivial gapped to Haldane gapped phase, as shown in Fig. 6(f), signifies a first-order transition (also see Fig. 5).

6. Central charge

Now we want to give numerical evidence for the central charge predicted by the bosonization analysis. We find the central charge (c) by fitting the bipartite von Neumann entanglement entropy (S_{vN}) to its conformal expression [62]

$$S_{vN} = \frac{c}{6} \ln \left[\frac{L}{\pi} \sin \frac{\pi l}{L} \right] + g. \quad (52)$$

Figure 8(a) show how c changes at the transition between XY_1 and XY_2 phases according to Fig. 5. In Fig. 8(b), we represent c along the $t = 0$ line that cuts through the interface between the XY_1 and XY_2 phases. As discussed above in the analytical analysis, we find from the numerical analysis, although not exactly, that the c is close to 2 in the $XY_1 - XY_1^*$ transition and at the Ising transition point between the phases XY_1 and XY_2 , the c is close to 1.5 (up to finite-size effects).

B. Characterising gapless phases

Since the gapped phases and particularly ordered phases are well understood and can be easily characterized by conventional order parameters, here we will focus our discussion on the gapless phases and their characterization.

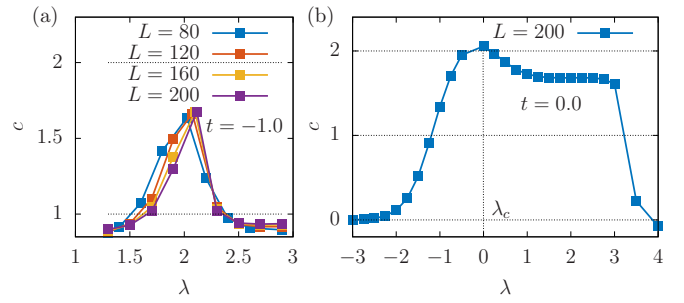


FIG. 8. The central charge (c) is plotted for cuts along (a) $t = -1.0$ that goes through the XY_1 and XY_2 phases for different L corresponding to Fig. 5 where $J = 2.5$ and $\Delta = 0.1$. In (b), we plot c for a system of $L = 200$ along a cut that goes through the interface between the phases XY_1 and XY_1^* ($t = 0$) (see Fig. 5).

1. String-order parameter

A particularly useful tool, which also helps in distillation of the topological features of the gapless phases, is the string-order parameter $C_{i,j}$ [see equivalently Eq. (19) up to a phase] where

$$C_{i,j} = -\langle z_i e^{i\frac{\pi}{2} \sum_{k=i+1}^{j-1} z_k} z_j \rangle, \quad (53)$$

and $z_i = 1 - 2b_i^\dagger b_i$. The string order parameter $|C_{2,L-1}|$, not unexpectedly, shows a finite value in the Haldane (gapped) phases in the system (not shown) [58,63]. Interestingly, the same order parameter also takes nontrivial values in XY_2^* , proving that it is a *gapless topological* phase. In Fig. 9(a) the behavior of $|C_{i,j}|$ is shown for both XY_2 (circles) and XY_2^* (squares)—one finds that, unlike XY_2 , in XY_2^* , $|C_{i,j}|$ takes a finite value that does not decay with $|i - j|$. Similarly in Fig. 9(b) we plot $|C_{i,j}|$ within the phase XY_1 (circles) and XY_1^* (squares), and in Fig. 9(c), we plot it in the XY_0 phase. In both plots, the string order parameter vanishes, showing that these phases are trivial in nature.

2. Local order parameters

The nature of long-range correlations can also distinguish between the different phases, as shown in Table VI. To this end, we calculate $|\langle O_i^{s+} O_j^{s-} \rangle|$ and $|\langle O_i^{a+} O_j^{a-} \rangle|$ where $O_i^{s+} = b_{1,i}^\dagger + b_{2,i}^\dagger$ and $O_i^{a+} = b_{1,i}^\dagger - b_{2,i}^\dagger$ to distinguish between the trivial, XY_1 , XY_1^* , and XY_2 phases. The results are shown in Figs. 9(d)–9(g) for all the gapless phases. We see a contrast in the nature of these correlations in two phases. The $|\langle O_i^{s+} O_j^{s-} \rangle|$ ($|\langle O_i^{a+} O_j^{a-} \rangle|$) falls exponentially (algebraically) with distance $|i - j|$ in the XY_1 phase. Whereas, in the XY_1^* phase, the behavior flips. However, in XY_0 and XY_2 , both correlation functions are algebraic or exponential, as shown in Figs. 9(f) and 9(g), respectively.

3. Edge states

The topological XY_2^* phase exhibits edge states, a hallmark property of such topological phases. In Figs. 10(a) and 10(b), we plot the number of particles $n_{r,i} = \langle n_{1,i} + n_{2,i} \rangle$ in strong rungs, where the hopping and interaction coupling are large (even or odd rungs) according to the construction of the system, for the phases XY_2 and XY_2^* , respectively. For XY_2^* ,

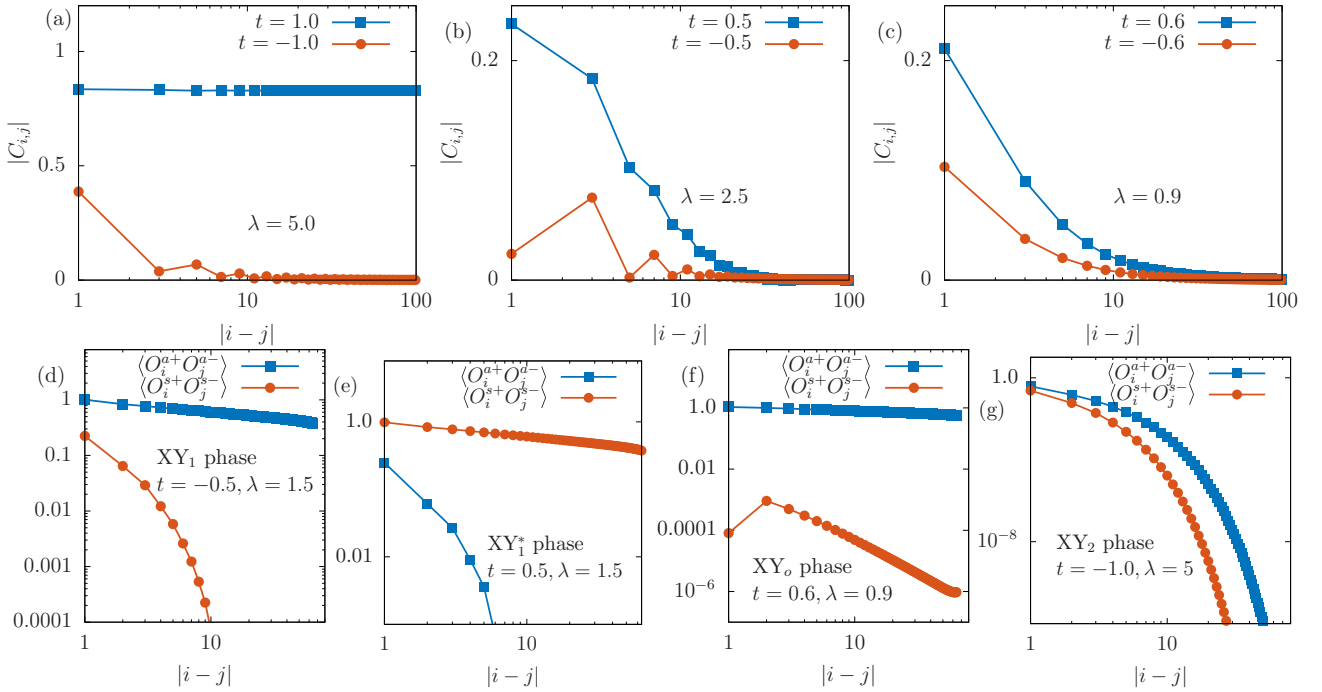


FIG. 9. String order parameter $|C_{i,j}|$ is shown in (a)–(c) for different gapless phases to distinguish the trivial and nontrivial topological phases. (a) The parameter $(\lambda, t) = (5, -1.0)$ belongs to the XY_2 phase and $(5, 1.0)$ belongs to the XY_2^* phase (see Fig. 5). The presence (absence) of long-range $|C_{i,j}|$ signifies the nontrivial (trivial) topological nature of the XY_2^* (XY_2) phase. (b) The parameter $(2.5, -0.5)$ belongs to the XY_1 phase and $(2.5, 0.5)$ belongs to the XY_1^* phase (see Fig. 5). The absence of long-range $|C_{i,j}|$ signifies the trivial nature of the phases XY_1 and XY_1^* . (c) $|C_{i,j}|$ for the XY_0 phase ($J = 0$) [see Fig. 4(a)]. For all cases, we calculate C_{ij} with $i = L/4 + 1$, and j goes from $\frac{L}{4} + 2$ to L where $j - i \in \text{odd}$ for a system of $L = 200$. [(d)–(g)] The correlation functions $|\langle O_i^+ O_j^- \rangle|$ (circles) and $|\langle O_i^{a+} O_j^{a-} \rangle|$ (squares) as a function of distance $|i - j|$ for four different gapless phases XY_1 , XY_1^* , XY_0 , and XY_2 , respectively. (g) Also applicable to XY_2^* . We see different behaviors of these correlations in different gapless phases (see the main text). Note that in (d), (e), and (g), the parameters correspond to the phases in Fig. 5, and the parameters in (f) correspond to the phase in Fig. 4(a). Here, we also use a system of $L = 200$ and calculate the correlations at the center of the system where $i = L/8$.

two edge sites do not belong to the strong bond where we plot $\langle n_i \rangle$. We can see that, only for the XY_2^* phase [Fig. 10(b)], the system exhibits exponentially localized occupied edge states.

The edge states manifest gapless excitations at the edges of the system. To confirm this property, we plot the energy gap for the excitation [Eq. (50)] at half-filling. In Fig. 11

we plot ΔE_L for $\Delta n = 1$ (circles) and $\Delta n = 2$ (triangles) in the phases XY_2 (solid symbols) and XY_2^* (empty symbols). In both phases, the elementary excitation in bulk is $\Delta n = 2$ (a pair of particles on the strong rungs), which is gapless. This can be confirmed from the algebraic decay of ΔE_L . In the XY_2^* phase, due to the presence of edge states, which can be

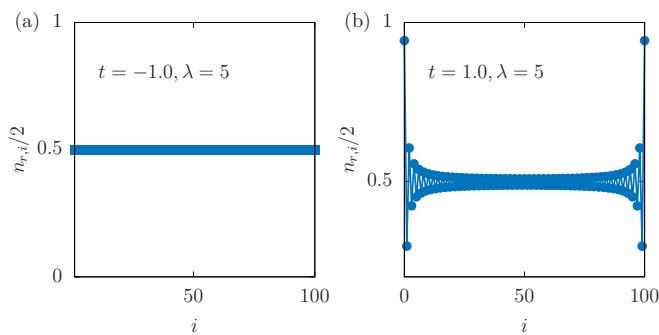


FIG. 10. The presence of edge state in the topological gapless phase (XY_2^*), which is present in phase diagram Fig. 5, is portrayed. Here, $J = 2.5$ and $\Delta = 0.1$. (a) The density of particles $n_{r,i}/2$ on the rung i with stronger coupling is plotted corresponding to XY_2 phase and (b) the same except the edge sites where $\langle n_i \rangle$ is plotted corresponding to XY_2^* phase.

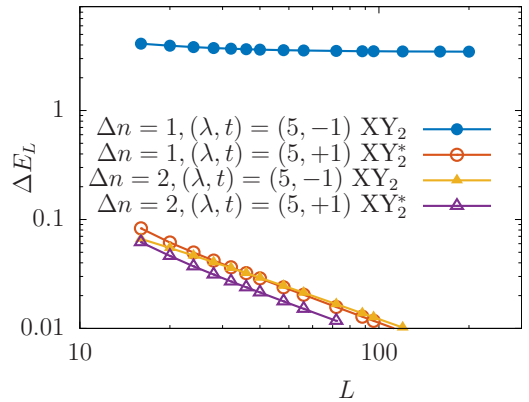


FIG. 11. The energy gaps ΔE_L is plotted for XY_2 (solid symbols) and XY_2^* (empty symbols) phases, emerged in Fig. 5, as a function of L . Circles and triangles represent single ($\Delta n = 1$) and two-particle ($\Delta n = 2$) excitation gaps, respectively. Here, $J = 2.5$ and $\Delta = 0.1$.

occupied by a single particle, we see algebraic decay of ΔE_L even with $\Delta n = 1$. In the XY_2 phase, however, single particle excitation is gapped where ΔE_L saturates to a finite value.

VI. MAPPING TO EFFECTIVE SPIN-1 MODELS

The connection between phase diagrams of spin- $\frac{1}{2}$ ladders and higher-spin chains is rather well known [40]. Certain parts of the phase diagram shown in Fig. 2 too can be determined using a mapping to an effective spin-1 model. This provides both consistency checks and physical insights into the phases. To do this, let us begin with the Hamiltonian in Eq. (2) and perform a change of basis

$$\begin{pmatrix} S_{1j}^x \\ S_{1j}^y \\ S_{1j}^z \end{pmatrix} \mapsto \begin{pmatrix} -S_{1j}^x \\ -S_{1j}^y \\ S_{1j}^z \end{pmatrix}, \quad \begin{pmatrix} S_{2j}^x \\ S_{2j}^y \\ S_{2j}^z \end{pmatrix} \mapsto \begin{pmatrix} S_{2j}^x \\ S_{2j}^y \\ S_{2j}^z \end{pmatrix}, \quad (54)$$

which results in the following change in H_\perp and H'_\perp :

$$\begin{aligned} H'_\perp &\mapsto -(1+t) \sum_j (S_{2j}^x S_{1j+1}^x + S_{2j}^y S_{1j+1}^y + \lambda S_{2j}^z S_{1j+1}^z), \\ H_\perp &\mapsto -(1-t) \sum_j (S_{1j}^x S_{2j}^x + S_{1j}^y S_{2j}^y + \lambda S_{1j}^z S_{2j}^z). \end{aligned} \quad (55)$$

Let us first consider the parameter regime when H_\perp is dominant, i.e., $t \approx -1$. Since H_\perp decouples into disjoint pieces each of which has support on two spins living on vertical bonds as shown in Fig. 12 and takes the form

$$h_\perp = -(1-t)(S_{1j}^x S_{2j}^x + S_{1j}^y S_{2j}^y + \lambda S_{1j}^z S_{2j}^z). \quad (56)$$

It can be easily diagonalized as follows (suppressing site labels for clarity):

$$\begin{aligned} h_\perp &= (1-t)[(\lambda+2)|s\rangle\langle s| + (\lambda-2)|0\rangle\langle 0| \\ &\quad - \lambda(|+1\rangle\langle +1| + |-1\rangle\langle -1|)] \text{ where} \\ |+1\rangle &\equiv |\uparrow_1 \uparrow_2\rangle, \quad |-1\rangle \equiv |\downarrow_1 \downarrow_2\rangle, \\ |0\rangle &\equiv \frac{|\uparrow_1 \downarrow_2\rangle + |\downarrow_1 \uparrow_2\rangle}{\sqrt{2}}, \quad |s\rangle \equiv \frac{|\uparrow_1 \downarrow_2\rangle - |\downarrow_1 \uparrow_2\rangle}{\sqrt{2}}, \end{aligned} \quad (57)$$

where $|\uparrow\rangle, |\downarrow\rangle$ represent eigenstates of S^z with eigenvalues $\pm\frac{1}{2}$ respectively. We see that for all values of $\lambda > -1$, $|\pm 1\rangle, |0\rangle$ have the lowest energies. We can project the two-spin Hilbert space on the vertical bonds of every site onto this three-dimensional subspace using the following projection operator:

$$\mathbb{P} = \prod_j (|0\rangle\langle 0| + |+1\rangle\langle +1| + |-1\rangle\langle -1|) \quad (58)$$

as schematically shown in the top panel of Fig. 12 to get an effective spin-1 chain with Hamiltonian

$$\begin{aligned} H_{eff} &= \mathbb{P} H \mathbb{P}^\dagger = J_{xy} \sum_j (L_j^x L_{j+1}^x + L_j^y L_{j+1}^y) \\ &\quad + J_z \sum_j L_j^z L_{j+1}^z + D \sum_j (L_j^z)^2 \end{aligned} \quad (59)$$

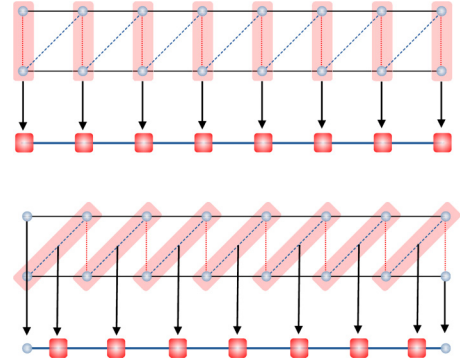


FIG. 12. Mapping to an effective spin-1 chain in the regime $t \approx -1$ (top) and $t \approx +1$ (bottom). Circles represent the qubits from the original Hilbert space and the boxes enclosing circles represent which pair of qubits are mapped to effective spin-1 entities (squares). Boundary effects are seen in the latter case where the mapping leaves behind a qubit on each end.

where

$$\begin{aligned} J_{xy} &= \left(\frac{J}{2} - \frac{(1+t)}{4} \right), \quad J_z = - \left(\frac{J\Delta}{2} + \frac{\lambda(1+t)}{4} \right), \\ \text{and } D &= 2(1-t)(1-\lambda). \end{aligned} \quad (60)$$

L^x, L^y, L^z are the spin-1 representations of the angular momentum algebra with representations

$$\frac{1}{\sqrt{2}} \begin{pmatrix} 0 & 1 & 0 \\ 1 & 0 & 1 \\ 0 & 1 & 0 \end{pmatrix}, \quad \frac{1}{\sqrt{2}} \begin{pmatrix} 0 & -i & 0 \\ i & 0 & -i \\ 0 & i & 0 \end{pmatrix}, \quad \begin{pmatrix} 1 & 0 & 0 \\ 0 & 0 & 0 \\ 0 & 0 & -1 \end{pmatrix}.$$

The Hamiltonian in Eq. (59) is the familiar spin-1 XXZ model with uniaxial single-ion-type anisotropy whose phase diagram is known [64] and is schematically reproduced in Fig. 13. For the parameter regime close to $t \approx -1$, the phases and transitions of the Hamiltonian in Eq. (2) are qualitatively reproduced by that of Eq. (59). For example, consider the limit $t \rightarrow -1$ when Eq. (59) reduces to

$$\begin{aligned} H_{eff} &\rightarrow \frac{J}{2} \sum_j (L_j^x L_{j+1}^x + L_j^y L_{j+1}^y - \Delta L_j^z L_{j+1}^z) \\ &\quad + 4(1-\lambda) \sum_j (L_j^z)^2. \end{aligned} \quad (61)$$

If Δ is fixed to a small value, as λ is tuned, we see from Fig. 13 that Eq. (61) passes through the large-D (trivial), XY_1 , XY_2 and the Ferromagnetic phases—the same as what is seen in Fig. 2. It is worth emphasizing the crucial role of Δ , which builds residual ferromagnetic correlations between effective spin-1's, thus leading to the realization of interesting gapless phases. Through the spin-1 mapping we are able to see that in order to access the XY_2 phase, we *need* to fix Δ to be small as was done in our numerical investigations.

Let us now consider the limit when the Hamiltonian Eq. (2) is dominated by H'_\perp . First, let us observe that with periodic boundary conditions, $t \mapsto -t$ is induced by a unitary transformation generated by a single-site translation on one of the legs of the ladder $\vec{S}_{1j} \mapsto \vec{S}_{1j+1}$. As a result, the phase diagram for Eq. (2) is perfectly symmetric under $t \mapsto -t$. The identity of

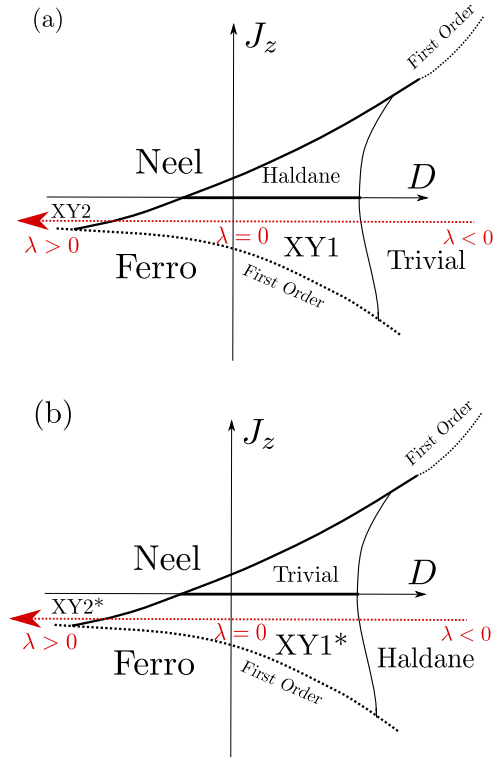


FIG. 13. Schematic phase diagrams of the spin-1 XXZ chain Hamiltonians shown in Eqs. (59) and (65) applicable to the limits $t \sim -1$ (top) and $t \sim +1$ (bottom) of Eq. (2) whose phase diagram is shown in Fig. 2.

the phases, however, can change under this map. In particular, the unitary transformation is ill defined with open boundary conditions and therefore it is conceivable that the distinction between the regions related by $t \mapsto -t$, is topological in nature. We will now map the H'_\perp dominant Hamiltonian to a spin-1 chain. To do this, we repeat the steps above and observe that with periodic boundary conditions, H'_\perp decouples into disjoint pieces, each of which has support on two spins, this time living on the diagonal bonds as schematically shown in the bottom panel of Fig. 12. We again perform a convenient change of basis similar to Eq. (55) to get the following local term:

$$h'_\perp = -(1+t)(S_{2j}^x S_{1j+1}^x + S_{2j}^y S_{1j+1}^y + \lambda S_{2j}^z S_{1j+1}^z).$$

This is easily diagonalized as

$$h'_\perp = (1+t)[(\lambda+2)|s\rangle\langle s| + (\lambda-2)|0\rangle\langle 0| - \lambda(|+1\rangle\langle +1| + |-1\rangle\langle -1|)] \quad (62)$$

where $|\pm 1\rangle$, $|0\rangle$ and $|s\rangle$ are as defined as in Eq. (57). Projecting onto the low-energy Hilbert space spanned by $|\pm 1\rangle$, $|0\rangle$ on each diagonal bond, we again get an effective spin-1 chain with the following Hamiltonian:

$$H'_{eff} = J'_{xy} \sum_{\tilde{j}} \left(L_{\tilde{j}}^x L_{\tilde{j}+1}^x + L_{\tilde{j}}^y L_{\tilde{j}+1}^y \right) + J'_z \sum_{\tilde{j}} L_{\tilde{j}}^z L_{\tilde{j}+1}^z + D' \sum_{\tilde{j}} \left(L_{\tilde{j}}^z \right)^2 \quad (63)$$

with

$$J'_{xy} = \left(\frac{J}{2} - \frac{(1-t)}{4} \right), \quad J'_z = - \left(\frac{J\Delta}{2} + \frac{\lambda(1-t)}{4} \right), \quad D' = 2(1+t)(1-\lambda). \quad (64)$$

We have denoted the bond between spins $(2, j)$ and $(1, j+1)$ by \tilde{j} . So far, Eq. (63) looks identical to Eq. (59) with the replacement $t \mapsto -t$. However, a change occurs with open boundary conditions. There is no natural association of the boundary qubits with any diagonal bond. As a result, it survives the the projection and remains as a qubit on the ends of the chain. The effective Hamiltonian with open boundary conditions is thus

$$H'_{eff} = J'_{xy} \sum_{\tilde{j}=1}^{L-1} \left(L_{\tilde{j}}^x L_{\tilde{j}+1}^x + L_{\tilde{j}}^y L_{\tilde{j}+1}^y \right) + J'_z \sum_{\tilde{j}=1}^{L-1} L_{\tilde{j}}^z L_{\tilde{j}+1}^z + D' \sum_{\tilde{j}=1}^L \left(L_{\tilde{j}}^z \right)^2 + H^\partial, \quad (65)$$

where J'_{xy} , J'_z and D' are the same as in Eq. (64). H^∂ is the effective boundary Hamiltonian,

$$H^\partial = J_{xy}^\partial (S_{11}^x L_1^x + S_{11}^y L_1^y + L_L^x S_{2L+1}^x + L_L^y S_{2L+1}^y) + J_z^\partial (S_{11}^z L_1^z + L_L^z S_{2L+1}^z) \quad (66)$$

where the coupling constants to the boundary qubits \tilde{S}_{11} and \tilde{S}_{2L+1} are

$$J_{xy}^\partial \equiv \left(\frac{J}{2} - \frac{(1-t)}{2} \right), \quad J_z^\partial = - \left(\frac{J\Delta}{2} + \frac{\lambda(1-t)}{2} \right).$$

The picture above suggests an interesting alternative method of analysis to the Abelian bosonization of Sec. III by treating the boundary spin-1/2 as a quantum impurity [65]; however, we will not pursue this route in this paper and leave it for future work.

Let us make a few comments on the limitations and utility of the mapping to a spin-1 chain before we proceed to a discussion of the phases in the effective Hamiltonian for the $t \sim 1$ limit. Recall that for the $t \sim 1$ limit, the phase diagram for the spin-1 XXZ chain accurately reproduces the phases of the spin ladder. To identify the phases of the spin-1 XXZ with that of Eq. (2) in the $t \sim -1$ limit, we need additional tools, although plausible arguments can be made, especially for the gapped phases. For instance, it is clear that the identity of the Ferromagnet obtained for large λ remains the same in Eqs. (65) and (59) as can be easily seen by taking λ to a large value in Eq. (2). The identities of the large-D and Haldane phase in Eq. (59) are reversed in Eq. (65) and can be understood from the effect of additional end qubits appearing with open boundary conditions. On the one hand, the qubit hybridizes with the edge mode of the Haldane phase and gaps out the edge degeneracy, rendering it a trivial phase. On the other hand, the same qubits contribute to the edge degeneracy to the large-D phase where the gapped bulk protects the hybridization between qubits on opposite ends of the chain, thus converting it to a topological phase. The effect of the qubits

on the gapless phases is not straightforward to determine. One could extend the previous argument to justify the mapping of the XY_2 phase to the topological XY_2^* phase, which has edge modes, but the absence of a bulk gap makes it heuristic at best. Indeed, the mapping of XY_1 to a different gapless phase XY_1^* , which does not have edge modes, is not easily explained within the spin-1 mapping. We need more sophisticated tools, such as bosonization and numerical analysis, to nail down the precise identity and nature of gapless phases, as has been achieved in the previous sections.

In summary, spin-1 mapping presents an independent confirmation of distinct phases in the limits $t \sim 1$. It also guides us to fix the parameters to open up various gapless phases, especially XY_2 . It also confirms that the topology of the $t \sim -1$ phase diagram is identical to that of $t \sim +1$. However, additional analysis, as has been shown in the previous sections, is needed to determine the identity of phases in the latter limit although heuristic arguments are consistent with detailed analysis.

VII. SUMMARY AND OUTLOOK

In this paper we have studied a coupled spin model hosting several symmetry-enriched gapless phases that exhibit an intricate interplay of symmetries, strong correlations, and topological features. Our multipronged approach, which includes bosonization (Secs. III and IV), DMRG studies (Sec. V), and effective low-energy modeling (Sec. VI) provides a comprehensive understanding of all aspects of the phase diagram. Our study points out that even the well-known Luttinger liquid state can appear in the form of distinct phases based on how the microscopic UV symmetries inherited from the underlying spin model get reflected in the low-energy IR (see Sec. III C). Among these phases is an interesting *gapless* topological phase XY_2^* that hosts symmetry-protected edge modes. Finally, our mapping to a Spin 1 XXZ chain (Sec. VI) provides an alternative view point to understand the nature of the gapless phases and their transitions. We also find the presence of multiple stable universality classes—“multiversality” along the critical surface separating the gapped trivial and Haldane phases.

There are many generalizations that can follow from our paper. First, it would be useful to use more sophisticated tools of boundary CFT [16,66] to gain insight into the gapless phases seen in this paper. Second, although in this paper we have focused on a two-chain ladder, we believe that as the number of chains increases, a much wider variety of symmetry-enriched criticality may be realizable in such systems, leading to a host of unique gapless phases and transitions [67,68]. Another interesting direction is to couple such one-dimensional chains to realize possibly novel two-dimensional gapless states [69–72] mimicking the success of gapped topological phases [73–76]. Finally, it would be interesting to see if the symmetry-enriched gapless phenomena investigated in this paper can be observed in Rydberg simulators [77] where other gapless phenomena have been postulated to exist [78–81]. We leave these and other questions to future work.

ACKNOWLEDGMENTS

We thank Masaki Oshikawa, Siddharth Parameswaran, Nick Bultinck, Sounak Biswas, Michele Fava, Nick Jones, Yuchi He, and Diptarka Das for useful discussions. We are especially grateful to Fabian Essler for collaboration in the early stages of this work. During the initial stages of this work, A.P. was supported by a grant from the Simons Foundation (677895, R.G.) through the ICTS-Simons post-doctoral fellowship. He is currently funded by the European Research Council under the European Union Horizon 2020 Research and Innovation Programme, Grant Agreement No. 804213-TMCS and the Engineering and Physical Sciences Research Council, Grant No. EP/S020527/1. S.M. acknowledges funding by the Deutsche Forschungsgemeinschaft (DFG, German Research Foundation) - 436382789, 493420525 via large-equipment grants (GOEGrid cluster). A.A. acknowledges support from IITK Initiation Grant (IITK/PHY/2022010). T.M. acknowledges support from DST-SERB, India through Project No. MTR/2022/000382. The authors acknowledge the hospitality of ICTS-TIFR, Bangalore, and ICTP, Trieste, where discussions and parts of this work were carried out.

APPENDIX A: ADDITIONAL BOSONIZATION DETAILS

The subject of bosonization has been extensively discussed in several excellent books and reviews. In this Appendix, we review a few details that are subtle and are easy to miss. The CFT term in Eqs. (3) and (7) is determined using standard techniques [35] from the XXZ Hamiltonian. The various perturbations can be determined from the bosonized form of the spin operators shown in Eqs. (5) and (9) in a straightforward manner for the most part. Cases involving coincident field operators should be treated with care employing a “point-splitting” device to determine how coincident vertex operators are multiplied. Let us review this in the single component/small- J limit,

$$\begin{aligned} e^{im\phi(x)} e^{in\theta(x)} &= \lim_{\epsilon \rightarrow 0} e^{im\phi(x+\epsilon)} e^{in\theta(x-\epsilon)} \\ &= \lim_{\epsilon \rightarrow 0} e^{i(m\phi(x+\epsilon)+n\theta(x-\epsilon))} e^{-\frac{mn}{2}[\phi(x+\epsilon), \theta(x-\epsilon)]} \\ &= \lim_{\epsilon \rightarrow 0} e^{in\theta(x-\epsilon)} e^{im\phi(x+\epsilon)} e^{-mn[\phi(x+\epsilon), \theta(x-\epsilon)]}. \end{aligned} \quad (\text{A1})$$

This is determined using an integrated version of Eqs. (4) and (8),

$$\begin{aligned} [\phi_\alpha(x), \theta_\beta(x')] &= i\pi \delta_{\alpha\beta} \text{sgn}(x-x'), \\ [\phi(x), \theta(x')] &= i\pi \text{sgn}(x-x'). \end{aligned} \quad (\text{A2})$$

using which we get

$$e^{im\phi(x)} e^{in\theta(x)} = (-1)^{mn} e^{in\theta(x)} e^{im\phi(x)}. \quad (\text{A3})$$

Equation (A3) is needed to obtain the correct bosonized form for operators involving products of S^\pm such as the bond-dimerization term $\propto \sum_j ((-1)^j S_j^+ S_{j+1}^- + \text{H.c.})$ in Eq. (1). Another important place where point splitting is needed is in determining the correct symmetry action. The $U(1)$, \mathbb{Z}_2^R , and \mathbb{Z} actions are easy to read off by directly comparing the action on the lattice operators shown in Table I with Eqs. (5) and (9).

The action of lattice parity \mathbb{Z}_2^R on the bosonized variables, on the other hand, needs some care. Let us review this again in the small- J , single-component version. Recall that the action of \mathbb{Z}_2^P is bond inversion, which can be thought of as a composite of site inversion and single-site translation. Since translation is straightforward by direct comparison, let us focus on site inversion $\vec{S}_j \mapsto \vec{S}_{-j}$. On the continuum operators and simple vertex operators, this naively acts as

$$\phi(x) \mapsto \phi(-x), \theta(x) \mapsto \theta(-x). \quad (\text{A4})$$

Let us look at how this naive action is reflected on products of noncommuting operators,

$$\begin{aligned} e^{im\theta(x)} e^{in\phi(x)} &= \lim_{\epsilon \rightarrow 0} e^{i\frac{mn\pi}{2} \text{sgn}(\epsilon)} e^{i(m\theta(x-\epsilon) + n\phi(x+\epsilon))} \\ &\mapsto \lim_{\epsilon \rightarrow 0} e^{i\frac{mn\pi}{2} \text{sgn}(\epsilon)} e^{i(m\theta(-x+\epsilon) + n\phi(-x-\epsilon))} \\ &= \lim_{\epsilon \rightarrow 0} e^{imn\pi \text{sgn}(\epsilon)} e^{im\theta(-x+\epsilon)} e^{in\phi(-x-\epsilon)} \\ &= (-1)^{mn} e^{im\theta(-x)} e^{in\phi(-x)}. \end{aligned} \quad (\text{A5})$$

Using Eqs. (A4) and (A5) we get

$$\begin{aligned} S_{-j}^{\pm} &\approx \exp(\pm i\theta(-x))((-1)^j \mathcal{A} - \mathcal{C} \cos \phi(x) + \dots), \\ S_{-j}^z &\approx \frac{1}{2\pi} \partial_x \phi(-x) + (-1)^j \mathcal{B} \sin \phi(-x) + \dots \end{aligned} \quad (\text{A6})$$

We can now read off the symmetry action corresponding to site reflection from Eq. (A6) as

$$\phi(x) \mapsto \pi - \phi(x), \theta(x) \mapsto \theta(-x). \quad (\text{A7})$$

Combining Eq. (A7) with the action of translation shown in Table II, we get the final effective action of \mathbb{Z}_2^R shown in Table II.

APPENDIX B: PHASE DIAGRAMS FROM BOSONIZATION

In this Appendix, we use bosonization to obtain the qualitative details of the phase diagrams shown in the main text in both the small- and large- J limits.

1. The small- J phase diagram

Let us write down the form of the Hamiltonian at small J shown in Eq. (1)

$$\begin{aligned} H &= \sum_j (1 + (-1)^j t) (S_j^x S_{j+1}^x + S_j^y S_{j+1}^y - \lambda S_j^z S_{j+1}^z) \\ &+ J \sum_j (S_j^x S_{j+2}^x + S_j^y S_{j+2}^y - \Delta S_j^z S_{j+2}^z), \end{aligned} \quad (\text{B1})$$

and its bosonized version shown in Eq. (3),

$$\begin{aligned} H &\approx \frac{v}{2\pi} \int dx \left[\frac{1}{4K} (\partial_x \phi)^2 + K (\partial_x \theta)^2 \right] \\ &+ 2\mathcal{A}ct \int dx \cos \phi - \frac{\mathcal{B}^2 \lambda}{2} \int dx \cos 2\phi + \dots \end{aligned} \quad (\text{B2})$$

The Luttinger parameter K and velocity v depend on Hamiltonian parameters and can be determined from the Bethe ansatz solution of the XXZ spin chain [36]

$$K = \frac{\pi}{2 \arccos \lambda}, \quad v = \frac{K}{(2K-1)} \sin\left(\frac{\pi}{2K}\right). \quad (\text{B3})$$

Let us comment on a few limits of Eq. (B1). If we switch off both the nnn coupling J and dimerization t , we have the XXZ model, which can be solved by Bethe ansatz [82–84] with the phases shown in the $t = 0$ line of the figure in Fig. 2. The phase diagram with $t \neq 0$ and $J \neq 0$ can be easily understood as a perturbation of the XXZ spin chain [24] using the bosonized Hamiltonian shown in Eq. (B2). This is done by tracking the relevance (in the RG sense) of the two vertex operators $\cos \phi$ and $\cos 2\phi$, which have scaling dimensions K and $4K$, respectively, as follows.

The XY₀ phase. In the regime when $K > 2$, which corresponds to $\frac{1}{\sqrt{2}} < \lambda < 1$ from the formula in Eq. (B3), both $\cos \phi$ and $\cos 2\phi$ are irrelevant, and we get a gapless phase XY₀.

The Haldane and trivial phases. When $\frac{1}{2} < K < 2$, which corresponds to $-1 < \lambda < \frac{1}{\sqrt{2}}$, $\cos \phi$ is relevant while $\cos 2\phi$ is irrelevant. Therefore, we get gapped phases for $t \neq 0$ where $\langle \phi \rangle \rightarrow \pi$ for $t > 0$ corresponds to the Haldane phase and $\langle \phi \rangle \rightarrow 0$ for $t < 0$ corresponds to the trivial phase.

The Néel phase. When $K < \frac{1}{2}$, which corresponds to $\lambda < -1$, both $\cos \phi$ and $\cos 2\phi$ are relevant. When $\cos 2\phi$ is dominant (e.g., when $t = 0$), we get a Néel phase with $\langle \phi \rangle \rightarrow \pm \frac{\pi}{2}$. The transition between the Haldane/trivial phase and Néel phase is second-order and corresponds to the Ising universality class. See [85] for an explanation of this.

The ferromagnet. As $\lambda \rightarrow 1$, we get $K \rightarrow \infty$ and $v \rightarrow 0$ and the Luttinger liquid description becomes invalid as the system transitions to a ferromagnet through a first-order transition.

Putting these various pieces together, we reproduce the topology of the small- J phase diagram seen for small t . This is shown in Fig. 14.

2. The large- J phase diagram

Let us now write down the Hamiltonian form appropriate for large J ,

$$\begin{aligned} H &= H_1 + H_2 + H_{\perp} + H'_{\perp}, \quad \text{where,} \\ H_{\alpha} &= J \sum_j (S_{\alpha j}^x S_{\alpha j+1}^x + S_{\alpha j}^y S_{\alpha j+1}^y - \Delta S_{\alpha j}^z S_{\alpha j+1}^z), \\ H_{\perp} &= (1-t) \sum_j (S_{1j}^x S_{2j}^x + S_{1j}^y S_{2j}^y - \lambda S_{1j}^z S_{2j}^z), \\ H'_{\perp} &= (1+t) \sum_j (S_{2j}^x S_{1j+1}^x + S_{2j}^y S_{1j+1}^y - \lambda S_{2j}^z S_{1j+1}^z), \end{aligned} \quad (\text{B4})$$

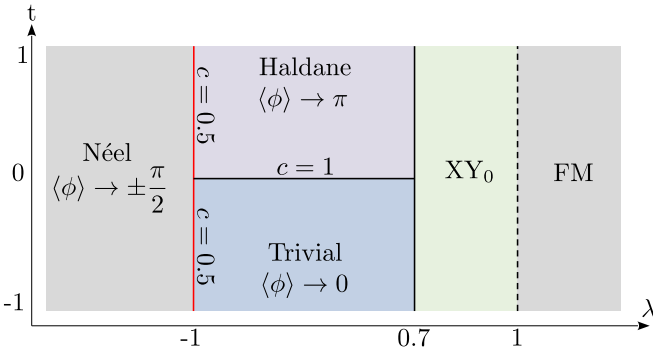


FIG. 14. The small- J phase diagram as determined from bosonization.

and its bosonized form

$$\begin{aligned}
 H \approx & \frac{v}{2\pi} \sum_{\alpha=1,2} \int dx \left(\frac{1}{4K} (\partial_x \phi_\alpha)^2 + K (\partial_x \theta_\alpha)^2 \right) \\
 & - \frac{\lambda}{2\pi^2} \int dx \partial_x \phi_1 \partial_x \phi_2 - 4A^2 t \int dx \cos(\theta_1 - \theta_2) \\
 & - \mathcal{B}^2 t \int dx \lambda (\cos(\phi_1 + \phi_2) - \cos(\phi_1 - \phi_2)) \\
 & + 2C^2 \int dx \cos(\theta_1 - \theta_2) \cos(\phi_1 + \phi_2) + \dots \quad (\text{B5})
 \end{aligned}$$

We now reproduce qualitative features of its diagram shown in Fig. 2. We will focus on the phases surrounding the $c = 2$ line over which we have good analytical control. The leading term in Eq. (B5) is a $c = 2$ CFT of two identical compact bosons. The operator $\partial_x \phi_1 \partial_x \phi_2$ has scaling dimensions 2 and is therefore exactly marginal. It generates motion in the space of $c = 2$ CFTs where the compact bosons are no longer identical and have different compactification radii. We also have operators $\mathcal{V}_\pm \equiv \cos(\phi_1 \pm \phi_2)$, $\mathcal{W}_- \equiv \cos(\theta_1 - \theta_2)$, and $\mathcal{W}_- \mathcal{V}_+ \equiv \cos(\theta_1 - \theta_2)(\phi_1 + \phi_2)$ whose scaling dimensions can be obtained perturbatively to the leading order in λ as [35]

$$\begin{aligned}
 [\mathcal{V}_\pm] &= K_\pm \approx 2K \left(1 \pm \frac{\lambda K}{\pi v} \right), \\
 [\mathcal{W}_-] &= \frac{1}{K_-} \approx \frac{1}{2K} \left(1 + \frac{\lambda K}{\pi v} \right), \text{ and} \\
 [\mathcal{W}_- \mathcal{V}_+] &= \frac{1}{K_-} + K_+ \approx \left(\frac{1}{2K} + 2K \right) \left(1 + \frac{\lambda K}{\pi v} \right), \quad (\text{B6})
 \end{aligned}$$

where, again, relationship of the Luttinger parameter K and velocity v with the parameters in the Hamiltonian is determined from the Bethe ansatz solution of the XXZ spin chain [36] as

$$K = \frac{\pi}{2 \arccos \Delta}, \quad v = \frac{JK}{(2K - 1)} \sin \left(\frac{\pi}{2K} \right). \quad (\text{B7})$$

Note that we have $[\mathcal{V}_-][\mathcal{W}_-] = 1$. As a result, it is impossible for both \mathcal{V}_- and \mathcal{W}_- to be irrelevant at the same time. Consequently, for any $t \neq 0$, the $c = 2$ theory is unstable and flows a gapless phase with $c < 2$ or a gapped phase [26,27,35] as seen in Fig. 2.

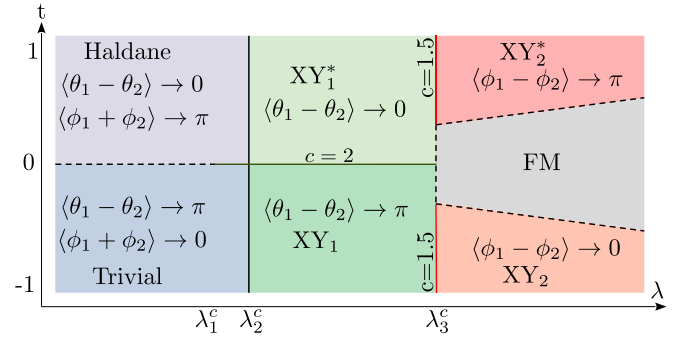


FIG. 15. The large- J phase diagram as determined from bosonization.

a. The phases and transitions

Let us begin in the limit $t \rightarrow 0$ in Eq. (B5) when $\mathcal{V}_+ \mathcal{W}_-$ is irrelevant, giving us a $c = 2$ theory. Recall that one of the two operators $\mathcal{W}_- \equiv \cos(\theta_1 - \theta_2)$ or $\mathcal{V}_- \equiv \cos(\phi_1 - \phi_2)$ is always relevant and, therefore, for $t \neq 0$, the theory flows to either a gapless state with $c < 2$ or gaps out completely. We are interested in the case where the system does not gap out completely, which occurs when $\mathcal{V}_+ \equiv \cos(\phi_1 + \phi_2)$ is irrelevant and the theory flows to effective single-component Luttinger liquid gapless phases. The nature of the phase depends on (i) which among \mathcal{W}_- and \mathcal{V}_- dominates at large distances, pinning $\theta_1 - \theta_2$ or $\phi_1 - \phi_2$ and (ii) the sign of t , which determines the value to which the fields are pinned $\langle \theta_1 - \theta_2 \rangle = 0/\pi$ or $\langle \phi_1 - \phi_2 \rangle = 0/\pi$. We label these four cases $XY_{1,2}$ and $XY_{1,2}^*$ as shown in Fig. 15. All four are distinct phases. The universality class of a direct continuous transition between $XY_{1/2}$ and $XY_{1/2}^*$ is the parent $c = 2$ theory obtained by tuning $t \rightarrow 0$. The transition between XY_1 and XY_2 or between XY_1^* and XY_2^* corresponds to a compact boson plus Ising CFT with central charge $c = \frac{3}{2}$ [23,40,86]. In the parameter regime we study the model numerically, a direct transition between XY_2 and XY_2^* is not observed.

When we are in the XY_1 or XY_1^* phases where \mathcal{W}_- pins the value of $\theta_1 - \theta_2$, a transition to a gapped phase can occur when \mathcal{V}_+ also becomes relevant. The gapped phases resulting when $\theta_1 - \theta_2$ and $\phi_1 + \phi_2$ are pinned correspond to the Haldane or trivial phase [27] as shown in Fig. 15. A different transition can occur when we are in any of the four gapless phases, $XY_{1,2}$ and $XY_{1,2}^*$ and the Luttinger velocity vanishes, resulting in a first-order transition to a FM similar to the single-component small- J case.

b. The $t = 0$ line and its proximate phases

We now analyze the $t = 0$ line and its proximity in detail. First, let us analyze which gapless phase results when $t \neq 0$ is switched on. This is determined by which operator \mathcal{W}_- or \mathcal{V}_- has the smaller scaling dimension. In the parameter regime we studied numerically, we only find the former situation as shown in Fig. 15. When \mathcal{V}_+ becomes relevant along with \mathcal{W}_- , we see that $t \neq 0$ results in gapped phases. Let us denote λ_2^c as the location along the $t = 0$ line when \mathcal{V}_+ is marginal, i.e., $[\mathcal{V}_+] = 2$ where the XY_1 to the trivial phase boundary and the XY_1^* to- Haldane phase boundary meets the $c = 2$ line at $t = 0$.

Now, as seen in Eq. (B5), the $c = 2$ theory is destroyed by either (i) the composite operator $\mathcal{W}_-\mathcal{V}_+$ becomes relevant leading to a gapped state with two degenerate vacua $\langle\phi_1 + \phi_2\rangle = \pi - \langle\theta_1 - \theta_2\rangle = 0/\pi$ or (ii) the Luttinger velocity for one of the sectors vanishes rendering the continuum description invalid and we get a first-order transition to a FM. Let us denote the critical values of λ that result in each of these as λ_1^c and λ_3^c respectively. From the perturbative result shown in Eq. (B6), we can get rough estimates for $\lambda_1^c - \lambda_3^c$ although these estimates are not very reliable when they result in large values of $|\lambda_k^c|$ where the validity of perturbation theory no longer holds.

The nature of the phase transition between the trivial and Haldane phases that occurs at $t = 0$ depends on whether we are at $\lambda < \lambda_1^c$ or $\lambda_1^c < \lambda < \lambda_2^c$. As shown in Fig. 15, the latter results in a first-order phase transition in which the vacua of the Haldane and the trivial phase are degenerate whereas the former results in a second-order transition with $c = 2$. Putting all this together, we get the form shown in Fig. 16.

c. Multiversality

A curious observation is that although the small- J and large- J gapped Haldane and trivial phases are adiabatically connected, the nature of the second-order transitions between them is different at small J and large J . For small J , it is a $c = 1$ critical theory whereas for large J it is $c = 2$. Both are obtained by tuning a single parameter and are therefore generic. This phenomenon, called multiversality, has received attention in recent studies [22,23] although microscopic models that exhibit them are rare.

d. A nice possible proximate phase diagram

In the parameter regime when \mathcal{V}_+ is irrelevant, we previously argued that close to the $t = 0$ line $t \neq 0$ resulted in a gapless XY_1 or ($t < 0$) XY_1^* ($t > 0$) phases if $[\mathcal{W}_-] < [\mathcal{V}_-]$ and XY_2 ($t < 0$) or XY_2^* ($t > 0$) phases if $[\mathcal{W}_-] > [\mathcal{V}_-]$. If the $c = 2$ theory survived as $[\mathcal{W}_-] = [\mathcal{V}_-]$ (at some putative value λ_4^c , say) then it would open a direct transition between the phases XY_2 and XY_2^* . The $c = \frac{3}{2}$ lines discussed previously that separated the phases XY_1 and XY_2 ($t < 0$) and XY_1^* and XY_2^* ($t > 0$) would meet the line $t = 0$ at this point λ_4^c . Alternatively, the gapless theory becomes unstable before this can happen, giving us the situation shown in Fig. 15, which we observe in our numerical investigation. We postulate that there is some proximate parameter regime of our microscopic Hamiltonian where $\lambda_3^c > \lambda_4^c$ can be realized. In this case, we should see a phase diagram as shown in Fig. 16, which contains all the same phases as in Fig. 15 but also a direct transition between XY_2 and XY_2^* .

APPENDIX C: BOSONIZING STRING OPERATORS

1. Bosonizing $C(x, y)$ for small J

Bosonizing string order parameters is known to be tricky and rife with ambiguities [87,88]. Let us try to naively apply Eq. (5) to bosonize the string operator in Eq. (19) in the small- J limit,

$$C(x, y) \propto e^{\pm i\pi \sum_{l=x}^y S_l^z} \sim e^{\pm \frac{i}{2} \int_x^y ds \partial_s \phi(s)} \sim e^{\pm \frac{i}{2} (\phi(x) - \phi(y))}. \quad (\text{C1})$$

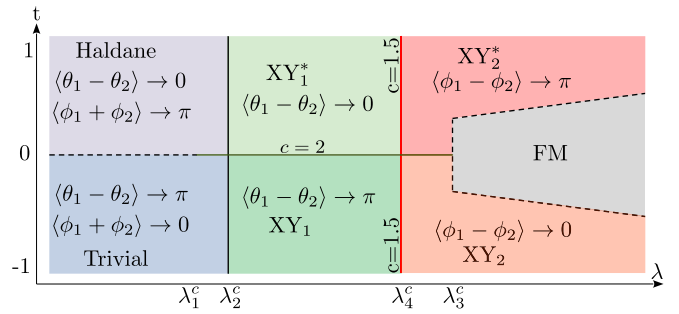


FIG. 16. A nice proximate phase diagram at large J suggested by bosonization.

Equation (C1) leads to the conclusion that $\langle C(x, y) \rangle \neq 0$ anytime $\langle \phi \rangle \neq 0$, in particular both in the Haldane and in the trivial phases. This is incorrect. We now use symmetries to identify the correct bosonized form of $C(x, y)$. We begin by postulating the following general bosonized form for $C(x, y)$:

$$C(x, y) \sim C_L(x) C_R(y) \text{ where } , \quad (\text{C2})$$

$$C_{L/R}(x) \sim \sum_{m \in \mathbb{Z}} A_m^{L/R} e^{\frac{i}{2} m \phi(x)}. \quad (\text{C3})$$

While the form in Eq. (C9) appears as though the string operator $C(x, y)$ has been written in terms of local operators with support at x and y , this is not so. The half-integer prefactor to the fields $\frac{\phi_a}{2}$ ensures that the operators in $C_{L/R}$ are not part of the spectrum of local operators $\mathcal{X}_{m,n} \equiv \exp(i(m\theta + n\phi))$ and are therefore nonlocal. Furthermore, we have used the fact that $C(x, y)^2 = 1$ to restrict the coefficients to multiples of $\frac{1}{2}$. We now impose constraints on $A_m^{L/R}$ using symmetry. First, observe that the endpoints of $C(x, y)$ defined in terms of spin operators as shown in Eq. (19) are charged under \mathbb{Z}_2^R ($S_j^z \mapsto -S_j^z$). Using the action of \mathbb{Z}_2^R on the boson fields shown in Table II, we obtain a constraint on $A_m^{L/R}$ as

$$\mathbb{Z}_2^R : C_{L/R} \xrightarrow{\phi \mapsto -\phi} -C_{L/R} \Rightarrow A_m^{L/R} = -A_{-m}^{L/R}. \quad (\text{C4})$$

We now impose the action of \mathbb{Z}_2^P shown in Table VII on the bosonized form of $C(x, y)$ using Table II, which gives a relationship between A_m^L and A_m^R as

$$\mathbb{Z}_2^P : C_L(x) \xrightarrow{\phi(x) \mapsto -\phi(-x)} C_R(-x) \Rightarrow A_m^R = A_{-m}^L = -A_m^L. \quad (\text{C5})$$

Using Eqs. (C4) and (C5) in Eq. (C3), we get the final bosonized form for $C(x, y) \sim C_L(x) C_R(y)$ with $C_L(x) = -C_R(x)$ and

$$C_L \sim \sum_{m \in \mathbb{Z}^+} \alpha_m \sin\left(\frac{m\phi}{2}\right) \approx \alpha_1 \sin\left(\frac{\phi}{2}\right), \quad (\text{C6})$$

where the coefficients α_m are linear combinations of $A_m^{L/R}$. This correctly reproduces the numerically observed behavior of $\langle C(x, y) \rangle$, which is nonzero when $\langle \phi \rangle = \pi$ such as in the Haldane phase but not when $\langle \phi \rangle = 0$ such as in the trivial phase.

2. Bosonizing $C(x, y)$ for large J

We now bosonize the string operator in the large- J version. We follow the same line of reasoning as shown previously for the small- J version. Let us begin by attempting to bosonize $C(x, y)$ using the formulas shown in Eq. (9),

$$\begin{aligned} C(x, y) &\propto e^{i\pi(\sum_{i=x}^{y-1} S_{1,i}^z + \sum_{i=x+1}^y S_{1,i}^z)} \sim e^{\frac{i}{2} \int_x^y ds \partial_s (\phi_1 + \phi_2)} \\ &\sim e^{\frac{i}{2}(\phi_1(x) + \phi_2(x))} e^{-\frac{i}{2}(\phi_1(y) + \phi_2(y))}. \end{aligned} \quad (\text{C7})$$

We may just as well have gone a different route to get

$$\begin{aligned} C(x, y) &\propto e^{i\pi(\sum_{i=x}^{y-1} S_{1,i}^z - \sum_{i=x+1}^y S_{1,i}^z)} \sim e^{\frac{i}{2} \int_x^y ds \partial_s (\phi_1 - \phi_2)} \\ &\sim e^{\frac{i}{2}(\phi_1(x) - \phi_2(x))} e^{-\frac{i}{2}(\phi_1(y) - \phi_2(y))}. \end{aligned} \quad (\text{C8})$$

The bosonized expressions in Eqs. (C7) and (C8) lead to very different physics. We have $\langle C(x, y) \rangle \neq 0$ when $\langle \phi_1 + \phi_2 \rangle \neq 0$ according to Eq. (C7) and when $\langle \phi_1 - \phi_2 \rangle \neq 0$ according to Eq. (C8), which corresponds to very different phases as seen in Fig. 15. Now we use symmetries to write down the correct bosonized form of $C(x, y)$. We again begin by postulating the following form for $C(x, y)$:

$$C(x, y) \sim C_L(x) C_R(y) \text{ where ,} \quad (\text{C9})$$

$$C_{L/R}(x) \sim \sum_{m,n \in \mathbb{Z}} A_{m,n}^{L/R} e^{\frac{i}{2}(m\phi_1(x) + n\phi_2(x))}. \quad (\text{C10})$$

We now impose constraints on $A_{m,n}^{L/R}$ using symmetry. First, we use the fact that the endpoints of $C(x, y)$ are charged under \mathbb{Z}_2^R ($S_{\alpha_j}^z \mapsto -S_{\alpha_j}^z$). Using the action of \mathbb{Z}_2^R on the boson fields shown in Table II, we get

$$\mathbb{Z}_2^R : C_{L/R}(x) \xrightarrow{\phi_\alpha \mapsto -\phi_\alpha} -C_{L/R}(x) \Rightarrow A_{m,n}^{L/R} = -A_{-m,-n}^{L/R}. \quad (\text{C11})$$

We now impose the action of \mathbb{Z}_2^P shown in Table VII on the bosonized form of $C(x, y)$ using Table II, which gives a relationship between A_{mn}^L and A_{mn}^R as

$$\begin{aligned} \mathbb{Z}_2^P : C_L(x) \xrightarrow{\phi_1(x) \mapsto \pm\pi - \phi_2(-x)} C_R(-x) \Rightarrow \\ A_{m,n}^R = \pm(i)^{m+n} A_{-n,-m}^L = \mp(i)^{m+n} A_{n,m}^L. \end{aligned} \quad (\text{C12})$$

Equations (C11) and (C12) are mutually compatible for nonzero A iff $(m+n)$ is even. Note that we have allowed a sign ambiguity in the action of \mathbb{Z}_2^P , $\phi_1 \mapsto \pm\pi - \phi_2$, which results in a harmless overall multiplicative sign factor in the final answer. Using these in Eq. (C10), we obtain the final bosonized form of $C(x, y) \sim C_L(x) C_R(y)$ with $C_L(x) = \pm C_R(y)$ and

$$C_L \approx \alpha \sin\left(\frac{\phi_1 + \phi_2}{2}\right) + \beta \sin\left(\frac{\phi_1 - \phi_2}{2}\right), \quad (\text{C13})$$

where we have only shown operators with the smallest scaling dimensions and the coefficients α, β are linear combinations

of $A_{m,n}^{L/R}$. This reproduces the observations in Sec. V that $\langle C(x, y) \rangle \neq 0$ when $\langle \phi_1 \pm \phi_2 \rangle = \pi$, i.e., in the Haldane and XY_2^* phases.

3. Bosonizing $U(\pi)$

We can obtain the bosonized form of the symmetry operator $U(\pi)$ defined on a finite interval $x \in [0, L]$, used in the main text using arguments similar to the above by treating it as a string operator defined for any interval. In the small- J limit, we can postulate the following form:

$$U(\pi) \sim U_L U_R, \quad (\text{C14})$$

$$U_{L/R} \sim \sum_m B_m^{L/R} e^{\frac{i}{2} m \phi}. \quad (\text{C15})$$

Unlike $C(x, y)$, which has \mathbb{Z}_2^R charged endpoints, $U_{L/R}$ do not carry any charge. Thus, we have

$$\mathbb{Z}_2^R : U_{L/R} \xrightarrow{\phi \mapsto -\phi} U_{L/R} \Rightarrow B_m^{L/R} = B_{-m}^{L/R}. \quad (\text{C16})$$

Imposing the action under \mathbb{Z}_2^P , we get

$$\mathbb{Z}_2^P : U_L(x) \xrightarrow{\phi(x) \mapsto -\phi(-x)} U_R(-x) \Rightarrow B_m^R = B_{-m}^L = B_m^L. \quad (\text{C17})$$

Using Eqs. (C16) and (C17), we get

$$U_{L/R} \sim \beta \cos\left(\frac{\phi}{2}\right) + \dots \quad (\text{C18})$$

where we have shown only the operator with the smallest scaling dimensions, and β is some combination of $B_m^{L/R}$. In the large- J limit, we can postulate the form

$$U(\pi) \sim U_L U_R, \quad (\text{C19})$$

$$U_{L/R} \sim \sum_{m,n} B_{m,n}^{L/R} e^{\frac{i}{2}(m\phi_1(x) + n\phi_2(x))}. \quad (\text{C20})$$

Again, imposing \mathbb{Z}_2^R invariance of the endpoints, we get

$$\mathbb{Z}_2^R : U_{L/R}(x) \xrightarrow{\phi_\alpha \mapsto -\phi_\alpha} U_{L/R}(x) \Rightarrow B_{m,n}^{L/R} = B_{-m,-n}^{L/R}. \quad (\text{C21})$$

The action of \mathbb{Z}_2^P further gives us

$$\begin{aligned} \mathbb{Z}_2^P : B_L(x) \xrightarrow{\phi_1(x) \mapsto \pm\pi - \phi_2(-x)} B_R(-x) \Rightarrow \\ B_{m,n}^R = \pm(i)^{m+n} B_{-n,-m}^L = \pm(i)^{m+n} B_{n,m}^L. \end{aligned} \quad (\text{C22})$$

Again, Eqs. (C21) and (C22) are mutually compatible for nonzero B iff $(m+n)$ is even and we have retained the sign ambiguity in the action of \mathbb{Z}_2^P as before when we bosonized $C(x, y)$. Using these in Eq. (C14), we get the final form $U(\pi) \sim U_L U_R$ with $U_L = \pm U_R$ and

$$U_L \approx \gamma \cos\left(\frac{\phi_1 + \phi_2}{2}\right) + \delta \cos\left(\frac{\phi_1 - \phi_2}{2}\right), \quad (\text{C23})$$

where we have only shown operators with the smallest scaling dimensions, and the coefficients γ, δ are linear combinations of $B_{m,n}^{L/R}$.

[1] L. D. Landau and E. M. Lifshitz, *Statistical Physics*, Vol. 5 (Elsevier, Amsterdam, 2013)

[2] X.-G. Wen, Topological orders in rigid states, *Int. J. Mod. Phys. B* **04**, 239 (1990).

- [3] M. E. Cage, K. Klitzing, A. Chang, F. Duncan, M. Haldane, R. B. Laughlin, A. Pruisken, and D. Thouless, *The Quantum Hall Effect* (Springer Science & Business Media, New York, 2012).
- [4] F. D. M. Haldane, Nobel lecture: Topological quantum matter, *Rev. Mod. Phys.* **89**, 040502 (2017).
- [5] E. M. Lifshitz and L. P. Pitaevskii, *Statistical Physics: Theory of the Condensed State*, Vol. 9 (Elsevier, Amsterdam, 2013).
- [6] T. Wehling, A. Black-Schaffer, and A. Balatsky, Dirac materials, *Adv. Phys.* **63**, 1 (2014).
- [7] A. Burkov, Weyl metals, *Annu. Rev. Condens. Matter Phys.* **9**, 359 (2018).
- [8] S. Sachdev, Topological order, emergent gauge fields, and Fermi surface reconstruction, *Rep. Prog. Phys.* **82**, 014001 (2019).
- [9] H. J. Schulz, Fermi liquids and non-Fermi liquids, in *Proceedings of Les Houches Summer School LXI*, edited by E. Akkermans, G. Montambaux, J. Pichard, and J. Zinn-Justin (Elsevier, Amsterdam, 1995), p. 533.
- [10] J. P. Kestner, B. Wang, J. D. Sau, and S. Das Sarma, Prediction of a gapless topological Haldane liquid phase in a one-dimensional cold polar molecular lattice, *Phys. Rev. B* **83**, 174409 (2011).
- [11] L. Fidkowski, R. M. Lutchyn, C. Nayak, and M. P. A. Fisher, Majorana zero modes in one-dimensional quantum wires without long-ranged superconducting order, *Phys. Rev. B* **84**, 195436 (2011).
- [12] M. Cheng and H.-H. Tu, Majorana edge states in interacting two-chain ladders of fermions, *Phys. Rev. B* **84**, 094503 (2011).
- [13] J. Ruhman, E. G. Dalla Torre, S. D. Huber, and E. Altman, Nonlocal order in elongated dipolar gases, *Phys. Rev. B* **85**, 125121 (2012).
- [14] A. Keselman and E. Berg, Gapless symmetry-protected topological phase of fermions in one dimension, *Phys. Rev. B* **91**, 235309 (2015).
- [15] T. Scaffidi, D. E. Parker, and R. Vasseur, Gapless symmetry-protected topological order, *Phys. Rev. X* **7**, 041048 (2017).
- [16] D. E. Parker, T. Scaffidi, and R. Vasseur, Topological Luttinger liquids from decorated domain walls, *Phys. Rev. B* **97**, 165114 (2018).
- [17] H.-C. Jiang, Z.-X. Li, A. Seidel, and D.-H. Lee, Symmetry protected topological Luttinger liquids and the phase transition between them, *Sci. Bull.* **63**, 753 (2018).
- [18] R. Verresen, R. Thorngren, N. G. Jones, and F. Pollmann, Gapless topological phases and symmetry-enriched quantum criticality, *Phys. Rev. X* **11**, 041059 (2021).
- [19] R. Thorngren, A. Vishwanath, and R. Verresen, Intrinsically gapless topological phases, *Phys. Rev. B* **104**, 075132 (2021).
- [20] F. D. M. Haldane, Luttinger liquid theory of one-dimensional quantum fluids. I. Properties of the Luttinger model and their extension to the general 1d interacting spinless Fermi gas, *J. Phys. C* **14**, 2585 (1981).
- [21] P. Ginsparg, Applied conformal field theory, in *Fields, Strings and Critical Phenomena*, edited by E. Brézin and J. Zinn-Justin, 1989 (Les Houches, Session XLIX, 1988).
- [22] Z. Bi and T. Senthil, Adventure in topological phase transitions in 3 + 1-D: Non-Abelian deconfined quantum criticalities and a possible duality, *Phys. Rev. X* **9**, 021034 (2019).
- [23] A. Prakash, M. Fava, and S. A. Parameswaran, Multiversality and unnecessary criticality in one dimension, *Phys. Rev. Lett.* **130**, 256401 (2023).
- [24] M. Kohmoto, M. den Nijs, and L. P. Kadanoff, Hamiltonian studies of the $d = 2$ Ashkin-Teller model, *Phys. Rev. B* **24**, 5229 (1981).
- [25] F. D. M. Haldane, Spontaneous dimerization in the $S = \frac{1}{2}$ Heisenberg antiferromagnetic chain with competing interactions, *Phys. Rev. B* **25**, 4925 (1982).
- [26] S. P. Strong and A. J. Millis, Competition between singlet formation and magnetic ordering in one-dimensional spin systems, *Phys. Rev. Lett.* **69**, 2419 (1992).
- [27] E. Orignac and T. Giamarchi, Weakly disordered spin ladders, *Phys. Rev. B* **57**, 5812 (1998).
- [28] R. D. Somma and A. A. Aligia, Phase diagram of the XXZ chain with next-nearest-neighbor interactions, *Phys. Rev. B* **64**, 024410 (2001).
- [29] S. Hirata and K. Nomura, Phase diagram of $S = \frac{1}{2}$ XXZ chain with next-nearest-neighbor interaction, *Phys. Rev. B* **61**, 9453 (2000).
- [30] X.-F. Jiang, Q. Jiang, and D. Xing, Elementary excitation and ground-state properties of dimerized XXZ chain with frustration, *Physica Status Solidi (b)* **229**, 1451 (2002).
- [31] S. Furukawa, M. Sato, S. Onoda, and A. Furusaki, Ground-state phase diagram of a spin- $\frac{1}{2}$ frustrated ferromagnetic XXZ chain: Haldane dimer phase and gapped/gapless chiral phases, *Phys. Rev. B* **86**, 094417 (2012).
- [32] M. Sato, S. Furukawa, S. Onoda, and A. Furusaki, Competing phases in spin-1/2 J1-J2 chain with easy-plane anisotropy, *Mod. Phys. Lett. B* **25**, 901 (2011).
- [33] The $U(1)$ and \mathbb{Z}_2^R symmetries do not commute and together form the non-Abelian group $O(2) \cong U(1) \times \mathbb{Z}_2^R$.
- [34] X. Chen, Z.-C. Gu, and X.-G. Wen, Complete classification of one-dimensional gapped quantum phases in interacting spin systems, *Phys. Rev. B* **84**, 235128 (2011).
- [35] T. Giamarchi, *Quantum Physics in One Dimension*, International Series of Monographs on Physics (Clarendon Press, Oxford, 2004).
- [36] F. Haldane, Demonstration of the “Luttinger liquid” character of Bethe-ansatz-soluble models of 1-D quantum fluids, *Phys. Lett. A* **81**, 153 (1981).
- [37] P. Francesco, P. Mathieu, and D. Sénéchal, *Conformal Field Theory* (Springer Science & Business Media, New York, 2012).
- [38] Recall that a scaling operator \mathcal{O} is relevant in $d+1$ dimensions if its scaling dimensions satisfies $[\mathcal{O}] < d + 1$.
- [39] A. A. Nersisyan, A. O. Gogolin, and F. H. L. Eßler, Incommensurate spin correlations in spin-1/2 frustrated two-leg Heisenberg ladders, *Phys. Rev. Lett.* **81**, 910 (1998).
- [40] H. J. Schulz, Phase diagrams and correlation exponents for quantum spin chains of arbitrary spin quantum number, *Phys. Rev. B* **34**, 6372 (1986).
- [41] Y. He, D. M. Kennes, C. Karrasch, and R. Rausch, Terminable transitions in a topological fermionic ladder, [arXiv:2302.14085](https://arxiv.org/abs/2302.14085).
- [42] Y. He, D. Pekker, and R. S. K. Mong, One-dimensional repulsive Hubbard model with mass imbalance: Orders and filling anomaly, *Phys. Rev. B* **104**, 195126 (2021).
- [43] The two $U(1)$ symmetries also contains a well known mixed anomaly [89]. The full collection of symmetries of the compact boson CFT is larger and contains the group of conformal transformations as well as other generators that may not even form

- a group structure [90,91]. For our purposes, the ones listed in Eq. (11) that form G_{IR} are sufficient.
- [44] Note that lattice operators with $U(1)$ charge 2 such as $S_{1,j}^{\pm}, S_{2,j}^{\pm}$ will have algebraic correlations in XY_2 and XY_2^* phases as shown in [40].
- [45] L. Li, M. Oshikawa, and Y. Zheng, Symmetry protected topological criticality: Decorated defect construction, signatures and stability, [arXiv:2204.03131](https://arxiv.org/abs/2204.03131).
- [46] R. Wen and A. C. Potter, Bulk-boundary correspondence for intrinsically gapless symmetry-protected topological phases from group cohomology, *Phys. Rev. B* **107**, 245127 (2023).
- [47] Note that Eq. (43) that breaks \mathbb{Z}_2^R but preserves \mathbb{Z}_2^P can be introduced to eliminate XY_2^* but preserve the Haldane phase. But this is not interesting.
- [48] X. Chen, Z.-C. Gu, Z.-X. Liu, and X.-G. Wen, Symmetry protected topological orders and the group cohomology of their symmetry group, *Phys. Rev. B* **87**, 155114 (2013).
- [49] S. R. White, Density matrix formulation for quantum renormalization groups, *Phys. Rev. Lett.* **69**, 2863 (1992).
- [50] U. Schollwöck, The density-matrix renormalization group in the age of matrix product states, *Ann. Phys.* **326**, 96 (2011), january 2011 Special Issue.
- [51] U. Schollwöck, The density-matrix renormalization group, *Rev. Mod. Phys.* **77**, 259 (2005).
- [52] S. Yoshida and K. Okamoto, Phase diagram of spin-1/2 alternating ferromagnetic chain with XY-like anisotropy, *J. Phys. Soc. Jpn.* **58**, 4367 (1989).
- [53] T. Mishra, S. Greschner, and L. Santos, Frustration-induced supersolids in the absence of intersite interactions, *Phys. Rev. B* **92**, 195149 (2015).
- [54] S. Greschner and T. Mishra, Interacting bosons in generalized zigzag and railroad-trestle models, *Phys. Rev. B* **100**, 144405 (2019).
- [55] A. Dhar, M. Maji, T. Mishra, R. V. Pai, S. Mukerjee, and A. Paramekanti, Bose-Hubbard model in a strong effective magnetic field: Emergence of a chiral Mott insulator ground state, *Phys. Rev. A* **85**, 041602(R) (2012).
- [56] S. Mondal, S. Greschner, and T. Mishra, Three-body constrained bosons in a double-well optical lattice, *Phys. Rev. A* **100**, 013627 (2019).
- [57] T. Mishra, J. Carrasquilla, and M. Rigol, Phase diagram of the half-filled one-dimensional t - v - V' model, *Phys. Rev. B* **84**, 115135 (2011).
- [58] S. Mondal, A. Padhan, and T. Mishra, Realizing a symmetry protected topological phase through dimerized interactions, *Phys. Rev. B* **106**, L201106 (2022).
- [59] S.-J. GU, Fidelity approach to quantum phase transitions, *Int. J. Mod. Phys. B*, **244371** (2010).
- [60] M. Singh, S. Greschner, and T. Mishra, Anomalous pairing of bosons: Effect of multibody interactions in an optical lattice, *Phys. Rev. A* **98**, 023615 (2018).
- [61] S. Lahiri, S. Mondal, K. Pandey, and T. Mishra, Correlated photon pair propagation in circuit qed with superconducting processors, *Phys. Rev. A* **102**, 043710 (2020).
- [62] P. Calabrese and J. Cardy, Entanglement entropy and conformal field theory, *J. Phys. A: Math. Theor.* **42**, 504005 (2009).
- [63] K. Hida, Crossover between the Haldane-gap phase and the dimer phase in the spin-1/2 alternating Heisenberg chain, *Phys. Rev. B* **45**, 2207 (1992).
- [64] W. Chen, K. Hida, and B. C. Sanctuary, Ground-state phase diagram of $s = 1$ XXZ chains with uniaxial single-ion-type anisotropy, *Phys. Rev. B* **67**, 104401 (2003).
- [65] I. Affleck, Quantum impurity problems in condensed matter physics, [arXiv:0809.3474](https://arxiv.org/abs/0809.3474).
- [66] X.-J. Yu, R.-Z. Huang, H.-H. Song, L. Xu, C. Ding, and L. Zhang, Conformal boundary conditions of symmetry-enriched quantum critical spin chains, *Phys. Rev. Lett.* **129**, 210601 (2022).
- [67] D. C. Cabra, A. Honecker, and P. Pujol, Magnetization plateaux in n -leg spin ladders, *Phys. Rev. B* **58**, 6241 (1998).
- [68] D. C. Cabra, A. Honecker, and P. Pujol, Magnetization curves of antiferromagnetic Heisenberg spin- $\frac{1}{2}$ ladders, *Phys. Rev. Lett.* **79**, 5126 (1997).
- [69] R. Mukhopadhyay, C. L. Kane, and T. C. Lubensky, Sliding Luttinger liquid phases, *Phys. Rev. B* **64**, 045120 (2001).
- [70] S. L. Sondhi and K. Yang, Sliding phases via magnetic fields, *Phys. Rev. B* **63**, 054430 (2001).
- [71] V. J. Emery, E. Fradkin, S. A. Kivelson, and T. C. Lubensky, Quantum theory of the smectic metal state in stripe phases, *Phys. Rev. Lett.* **85**, 2160 (2000).
- [72] A. Vishwanath and D. Carpentier, Two-dimensional anisotropic non-Fermi-liquid phase of coupled Luttinger liquids, *Phys. Rev. Lett.* **86**, 676 (2001).
- [73] V. M. Yakovenko, Quantum Hall effect in quasi-one-dimensional conductors, *Phys. Rev. B* **43**, 11353 (1991).
- [74] T. Neupert, C. Chamon, C. Mudry, and R. Thomale, Wire deconstructionism of two-dimensional topological phases, *Phys. Rev. B* **90**, 205101 (2014).
- [75] T. Meng, T. Neupert, M. Greiter, and R. Thomale, Coupled-wire construction of chiral spin liquids, *Phys. Rev. B* **91**, 241106(R) (2015).
- [76] Y. Liu, N. Tantivasadakarn, K. Slagle, D. F. Mross, and J. Alicea, Assembling Kitaev honeycomb spin liquids from arrays of 1d symmetry protected topological phases, [arXiv:2305.11221](https://arxiv.org/abs/2305.11221).
- [77] M. Morgado and S. Whitlock, Quantum simulation and computing with Rydberg-interacting qubits, *AVS Quantum Science* **3**, 023501 (2021).
- [78] M. Tsitsishvili, T. Chanda, M. Votto, P. Fromholz, M. Dalmonte, and A. Nersesyan, Phase diagram of Rydberg-dressed atoms on two-leg square ladders: Coupling supersymmetric conformal field theories on the lattice, *Phys. Rev. B* **105**, 155159 (2022).
- [79] L. Eck and P. Fendley, From the XXZ chain to the integrable Rydberg-blockade ladder via non-invertible duality defects, [arXiv:2302.14081](https://arxiv.org/abs/2302.14081).
- [80] L. Eck and P. Fendley, Critical lines and ordered phases in a Rydberg-blockade ladder, [arXiv:2304.08484](https://arxiv.org/abs/2304.08484).
- [81] P. Fromholz, M. Tsitsishvili, M. Votto, M. Dalmonte, A. Nersesyan, and T. Chanda, Phase diagram of Rydberg-dressed atoms on two-leg triangular ladders, *Phys. Rev. B* **106**, 155411 (2022).
- [82] R. Orbach, Linear antiferromagnetic chain with anisotropic coupling, *Phys. Rev.* **112**, 309 (1958).
- [83] C. N. Yang and C. P. Yang, One-dimensional chain of anisotropic spin-spin interactions. I. Proof of Bethe's hypothesis for ground state in a finite system, *Phys. Rev.* **150**, 321 (1966).

- [84] C. N. Yang and C. P. Yang, One-dimensional chain of anisotropic spin-spin interactions. II. Properties of the ground-state energy per lattice site for an infinite system, *Phys. Rev.* **150**, 327 (1966).
- [85] G. Delfino and G. Mussardo, Non-integrable aspects of the multi-frequency Sine-Gordon model, *Nucl. Phys. B* **516**, 675 (1998).
- [86] P. Lecheminant, A. O. Gogolin, and A. A. Nersisyan, Criticality in self-dual Sine-Gordon models, *Nucl. Phys. B* **639**, 502 (2002).
- [87] E. H. Kim, G. Fáth, J. Sólyom, and D. J. Scalapino, Phase transitions between topologically distinct gapped phases in isotropic spin ladders, *Phys. Rev. B* **62**, 14965 (2000).
- [88] M. Nakamura, Identification of topologically different valence bond states in spin ladders, *Phys. B: Condens. Matter* **329-333**, 1000 (2003).
- [89] E. Fradkin, *Quantum Field Theory: An Integrated Approach* (Princeton University Press, Princeton, 2021).
- [90] R. Thorngren and Y. Wang, Fusion category symmetry II: Categoriosities at $c = 1$ and beyond, [arXiv:2106.12577](https://arxiv.org/abs/2106.12577).
- [91] Y. Choi, C. Córdova, P.-S. Hsin, H. T. Lam, and S.-H. Shao, Noninvertible duality defects in $3 + 1$ dimensions, *Phys. Rev. D* **105**, 125016 (2022).